Journal of Computational Physics 297 (2015) 1–29

Contents lists available at ScienceDirect

Journal of Computational Physics

www.elsevier.com/locate/jcp

A finite element method to compute three-dimensional equilibrium configurations of fluid membranes: Optimal parameterization, variational formulation and applications

Ramsharan Rangarajan *, Huajian Gao

School of Engineering, Brown University, Providence, RI 02912, USA

ARTICLE INFO

Article history:
Received 10 September 2014
Received in revised form 16 February 2015
Accepted 3 May 2015
Available online 12 May 2015

Keywords:
Biomembrane
Cell adhesion
Finite element method
Cell-nanoparticle interaction
Drug delivery

ABSTRACT

We introduce a finite element method to compute equilibrium configurations of fluid membranes, identified as stationary points of a curvature-dependent bending energy functional under certain geometric constraints. The reparameterization symmetries in the problem pose a challenge in designing parametric finite element methods, and existing methods commonly resort to Lagrange multipliers or penalty parameters. In contrast, we exploit these symmetries by representing solution surfaces as normal offsets of given reference surfaces and entirely bypass the need for artificial constraints. We then resort to a Galerkin finite element method to compute discrete C^1 approximations of the normal offset coordinate.

The variational framework presented is suitable for computing deformations of three-dimensional membranes subject to a broad range of external interactions. We provide a systematic algorithm for computing large deformations, wherein solutions at subsequent load steps are identified as perturbations of previously computed ones. We discuss the numerical implementation of the method in detail and demonstrate its optimal convergence properties using examples. We discuss applications of the method to studying adhesive interactions of fluid membranes with rigid substrates and to investigate the influence of membrane tension in tether formation.

1. Introduction

1.1. Background

Lipid bilayers are fluid-like membranes and a principal constituent in the boundaries of virtually all cells and intracellular organelles. While real biological structures are quite complex, lipid bilayers serve as a simple yet representative medium to understand important mechanical and chemical functions of cell and organelle boundaries. We are concerned here with designing finite element methods to simulate the mechanical behavior of lipid bilayers modeled as fluid membranes.

We adopt Helfrich's continuum mechanical model to describe the bending elasticity of fluid membranes [1]. The model relies on (i) the thickness of fluid membranes being 2–3 orders of magnitude smaller than its lateral dimensions (nanometers compared to microns), (ii) the fluidity of lipids within each monolayer, (iii) the large resistance of fluid membranes to

* Corresponding author.
E-mail addresses: rram@brown.edu (R. Rangarajan), huajian_gao@brown.edu (H. Gao).

http://dx.doi.org/10.1016/j.jcp.2015.05.001
0021-9991/

surface dilation, and (iv) their selective permeability to ions dissolved within the bulk fluid. The first observation permits describing a fluid membrane as a two-dimensional surface, akin to descriptions of thin elastic shells. The distribution of lipids along this surface is analogous to the field of directors within the context of a 1-director Cosserat shell theory. Lipid bilayers lack a reference configuration and offer no resistance to shear. More crucially, the fluidity assumption informs the constitutive law that the material symmetry group consists of local area (or density) preserving transformations. Consequently, the constitutive relation is defined exclusively in terms of the membrane's principal curvatures [2–4]. Helfrich's model for the bending elasticity of fluid membranes follows from including terms up to second order in the principal curvatures. The model is usually discussed and justified from more phenomenological perspectives [5] and has been favorably compared with numerous experiments [6,7]. Geometric constraints on the surface areas of fluid membranes and their enclosed volumes play a crucial role in determining their equilibrium configurations. The rationale behind these constraints is discussed in Section 2. The corresponding Lagrange multipliers are interpreted as the surface tension in the membrane and the pressure in the enclosed fluid, respectively.

The Euler–Lagrange equations asserting stationarity of the bending energy of a fluid membrane are a system of nonlinear fourth-order partial differential equations in the coordinates describing its surface [8,9]. Explicit resolution of these equations to compute the surface coordinates is not feasible in general, although special solutions have been derived for specific geometries, loads and under the assumption of small deformations, see [6] and references therein. In the special case of axisymmetric deformations, we recover a system of ordinary differential equations relating the pressure, surface tension and coordinates of the generating curve. Such a system can be solved using shooting [8,10] or collocation methods [11].

To compute general three-dimensional deformations of fluid membranes however, numerical methods rely on the variational structure of the problem rather than the Euler–Lagrange equations. The description adopted for the membrane surface is a crucial choice in these methods— it may be described implicitly, say as the zero level set of a function, or parametrically by choosing a local system of coordinates. Phase field methods are a prominent example of the former [12–14]. These methods explicitly compute an order parameter (the phase field), that undergoes a diffuse transition at the membrane surface over a prescribed length scale (ε). Phase field models are favored for the simplicity they afford in accommodating complex surface topologies [15]. A recurring dilemma however concerns their computational efficiency, since the problem of computing a two-dimensional surface is replaced by one of computing a phase field in three dimensions. A naïve discretization entails an alarmingly expensive $\mathcal{O}(\varepsilon^{-3})$ degrees of freedom for the phase field. Adaptive refinement based on error estimators is indispensable in practice [16].

The second family of methods explicitly compute a parametric representation for the membrane [17]. The reparameterization symmetries of the bending energy and constraint functionals, a consequence of the *fluidity* of the membrane, present a fundamental difficulty in choosing a coordinate system. Cartesian coordinates are a convenient and ubiquitous choice, although they do not constitute a proper coordinate system. In a numerical implementation, choosing such an improper coordinate system results in undesirable tangential motions, i.e., the so-called zero-energy-modes [18,19]. It is then necessary to perform mesh smoothing or node redistribution operations to retain the qualities of meshes used [20,21]. The situation is alleviated to some extent when viscosity of the fluid membrane is considered [22–24].

The dependence of the bending energy on membrane curvatures introduces additional challenges in designing numerical schemes. It necessitates C^1 interpolations for the unknown fields in both phase field and parametric finite element methods. Lagrange-type elements afford only C^0 discretizations and are hence inadequate for Galerkin approximations. Instead, mixed elements have been successfully used and analyzed [16,25–27]. Alternately, C^1 finite element spaces have been constructed using spline-based functions [23,28,29], maximum-entropy approximants [14], and spectral representations [30]. Subdivision surfaces commonly used in computer graphics applications are also a promising alternative [18]. Nevertheless, challenges remain in constructing smooth interpolations on adaptively refined grids and in accommodating boundary conditions/constraints.

1.2. Scope of the paper

We present a variational framework for computing equilibrium configurations of fluid membranes undergoing large three-dimensional deformations. The main ingredients in the method are the following:

(i) We introduce a novel constraint-free parameterization for fluid membranes. The parameterization defines a membrane as a *normal offset* of a given *reference surface*. The normal offset is a scalar field and defines a proper coordinate for the membrane, while the role of the reference surface may be interpreted as that of an initial guess for the solution surface. In contrast with the aforementioned parametric finite element methods, the proposed parameterization entirely avoid the issue of zero-energy-modes.

(ii) The bending energy, constraint functionals, and their linearizations are straightforward to evaluate in the chosen coordinate system. Equilibrium membrane configurations are then computed as stationary points of the constrained energy functional, without requiring the derivation of the Euler–Lagrange equations. Inextensibility of the membrane surface and conservation of the volume enclosed by it are enforced using scalar Lagrange multipliers.

(iii) The discrete variational principle is a Galerkin approximation. It consists in restricting the continuous formulation to a C^1 finite element space for the normal offset coordinate. The discretized weak form is a system of nonlinear algebraic equations. We resolve them using a Newton-type method by deriving consistent tangent operators.

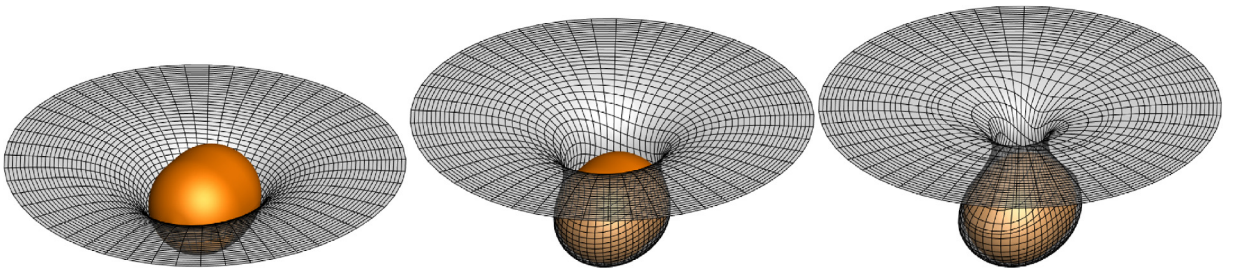

Fig. 1. A simulation showing the spontaneous adhesive uptake of a sphero-cylindrical particle by a fluid membrane, computed using the proposed finite element method. The example serves to illustrate the capability of the proposed method to simulate large, three-dimensional deformations of fluid membranes.

(iv) The set of computable membrane shapes are restricted to lie in the tubular neighborhood of the reference surface to ensure their regularity. Hence solution surfaces are assumed to be sufficiently small perturbations of the reference surface. This requirement is however not because of any approximations or linearizations of the material constitutive behavior. Large membrane deformations are computed through a sequence of incremental deformations, while updating the choice for the reference surface at each step, see Fig. 1.

The reparameterization symmetries of the bending energy and geometric constraint functionals can be interpreted as the stationarity of these functionals with respect to tangential variations. This fact, which motivates our choice of coordinate, has been widely recognized in the literature [31–33]. However, it does not appear to have been exploited in numerical methods for computing equilibrium membrane configurations. Indeed, as noted in [31], *the restriction to normal variations alone is not natural in mechanics*.

The remainder of the paper is organized as follows. First we recall the continuum model describing the bending elasticity of fluid membranes and the associated geometric constraints in Section 2. We discuss the kinematic description of a surface using offset coordinates and the resulting continuous/discrete variational problems in Section 3 and Section 4. We provide detailed expressions for evaluating the weak forms and derive consistent tangent operators for general three-dimensional solutions.

In a useful class of experimentally-relevant applications, it is reasonable to restrict membrane configurations to be axisymmetric. Such an assumption results in significant computational simplifications as well. In Section 6, we simulate the adhesive interaction of a vesicle with a rigid substrate, which is relevant to a commonly used experimental technique for characterizing the adhesion of vesicles to substrates. Then we consider the wrapping of a rigid spherical particle by a fluid membrane. Wrapping simulations are a useful step in studying the phenomenon of *endocytosis*, which is of interest to designing nano-particles for drug delivery [34–37] as well in investigating their potential toxic effects [38–40]. In Section 7, we examine the role of surface tension in the formation of tethers in fluid membranes. Besides their biological significance, tether formation is routinely exploited in experimental measurement techniques [41].

Finally, we mention that most of the numerical examples presented here required fewer than 10 Newton iterations for convergence at each load step. With stiff external interactions, such as the potential used in Section 6.3, a few additional iterations were required. We also observed that Newton iterations converged (at least) quadratically close to the solution. Such efficiency compares favorably with commonly used Monte Carlo methods for instance, that entail performing multiple simulations each requiring millions of flips of degrees of freedom to identify an equilibrium configuration.

2. Curvature elasticity with geometric constraints

We begin with a brief description of the model for the bending elasticity of fluid membranes and the associated geometric constraints.

2.1. Bending elasticity

The energy attributed to a configuration Υ of a fluid membrane, presumed to be a sufficiently smooth surface in $\mathbb{R}^3$, is given by

$$W[\Upsilon] := \frac{\kappa_b}{2}\int_{\Upsilon} (\mathrm{H}-C_0)^2\, d\Upsilon + \kappa_G \int_{\Upsilon} \mathrm{K}\, d\Upsilon, \tag{1}$$

where H and K are the mean and Gaussian curvatures, C_0 is termed a "spontaneous curvature", and κ_b and κ_G are the bending and Gaussian rigidities. Throughout this article, we shall ignore the possibility of membranes undergoing topology changes (e.g., fusion and rupturing). Consequently, the integral of the Gaussian curvature is a constant [42] and hence the

second term in (1) is ignored. The spontaneous curvature C_0 introduces an asymmetry, to reflect the distributions of certain lipids in the bilayer structure. For simplicity, we assume that $C_0 = 0$ throughout. We are hence left with the functional

$$\Pi_B[\Upsilon] := \frac{\kappa_b}{2} \int_{\Upsilon} \mathrm{H}^2 \, d\Upsilon, \tag{2}$$

which is also known as the Willmore energy. A few aspects of (2) are worth highlighting. First, the conspicuous absence of the thickness of the membrane is to be expected, since the thickness of biological membranes is typically many orders of magnitude smaller than their extent (nanometers compared to microns). Second, there is no information regarding the bilayer architecture of biological membranes/vesicles. Considering the in-plane deformations of each monolayer would introduce energetic contributions arising from gradients in density distributions of lipids in each layer, and in particular, signatures of the bilayer structure [6,43]. However, the bending rigidity is known to be much smaller than the in-plane elastic compression modulus, leading us to omit the latter. Finally, the absence of any resistance to shear in (2) reflects the distinction between fluid membranes and solid shells.

2.2. Geometric constraints for vesicles

Equilibrium shapes of fluid membranes are postulated to manifest as the result of a competition between the bending energy and geometric constraints on its surface area/volume. The rationale behind assuming a constant area, namely

$$\int_{\Upsilon} 1 \, d\Upsilon = \text{constant}, \tag{3}$$

comes from the observation that the low concentrations of free lipids in biological and experimental systems preclude the possibility of lipids being added or removed over any significant time scale. In addition to maintaining a roughly optimal number of lipids, a constant surface area also reflects the large resistance to in-plane elastic deformation. Constraint (3) explicitly distinguishes the bending elasticity of fluid membranes from that of material interfaces, whose behavior is governed predominantly by surface tension.

The constraint of constant volume,

$$\int_{\Omega} 1 \, d\Omega = \text{constant}, \tag{4}$$

where Ω is the volume bound by (a closed surface) Υ, is also sometimes assumed in the study of vesicles. The justification in this case comes from the impermeability of vesicle walls to ions/sugars dissolved in the ambient and enclosed fluids. Changes in volume of the vesicle would create osmotic pressures that would be too large to be sustained by just the elasticity of its boundary.

The Lagrange multipliers used to impose constraints (3) and (4) are interpreted as the membrane tension and pressure differential respectively.

2.3. External interactions

In addition to prescribed boundary conditions, we consider external interactions of the form

$$\Pi_F[\Upsilon] := \int_{\Upsilon} \mu \, d\Upsilon, \tag{5}$$

where $\mu : \mathbb{R}^3 \to \mathbb{R}$ represents the intensity of an external potential. A broad range of experimentally-relevant interactions are conveniently represented using (5). We provide specific examples for the case of adhesive interactions in Section 6.

3. Variational formulation with offset surfaces

We introduce a model problem for computing the parametric representation of an equilibrium configuration of a three-dimensional fluid membrane. To arrive at a well-posed problem, we restrict the family of admissible solutions to consist of normal offsets of a given reference surface. The resulting variational problem is free from artificial constraints and amenable to a simple Galerkin approximation discussed in Section 4. We provide detailed expressions to evaluate the weak form and derive the corresponding consistent tangent operators to be used in iterative numerical solution schemes.

3.1. A model problem

Consider the family of regular orientable surfaces parameterized over a given bounded set $\mathcal{A} \subset \mathbb{R}^2$

$$\mathcal{G} := \{\gamma = \{\boldsymbol{\varphi}(\boldsymbol{\xi}) : \boldsymbol{\xi} \in \mathcal{A}\}, \boldsymbol{\varphi} \in \mathbf{V}\}, \tag{6}$$

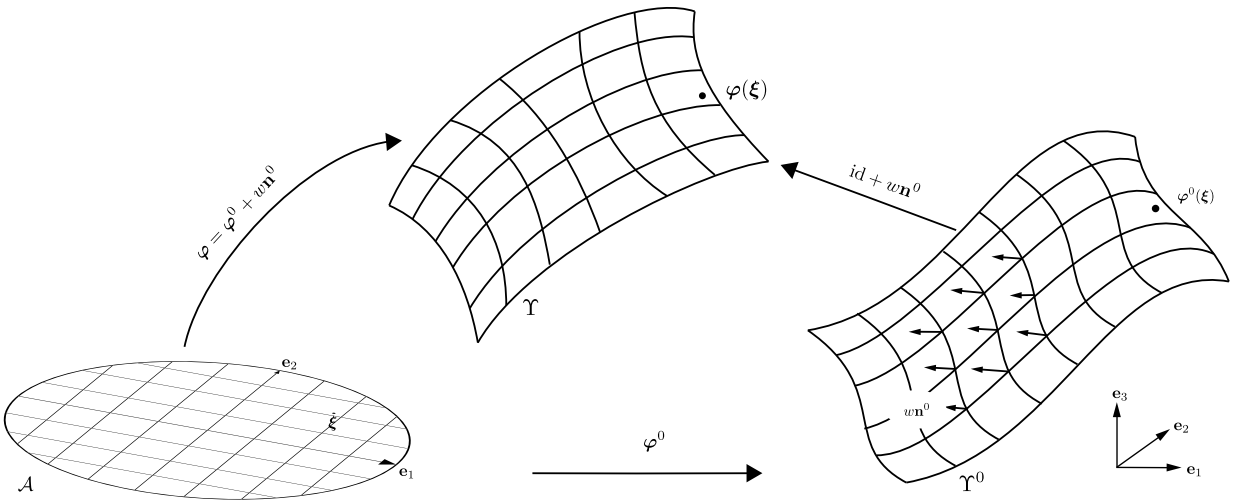

Fig. 2. Geometry of a membrane Υ represented as the normal offset of a reference surface Υ^0.

where we assume that $\mathbf{V} \subset [H^2(\mathcal{A})]^3$ incorporates the conditions for regularity, orientability and prescribed boundary conditions, and $H^2(\mathcal{A})$ is the Sobolev space of functions on the set $\mathcal{A}$. In general, and for closed surfaces in particular, a collection of charts is required in (6). The following discussion is easily adapted to the case of multiple charts and in favor of notational simplicity, we assume a single chart in (6).

We consider a model problem for computing $\Upsilon \in \mathcal{G}$ that is a stationary point of $\Pi_B + \Pi_F$ subject to the constraint of a given surface area A_0:

$$\boxed{\text{Find } \Upsilon = \{\boldsymbol{\varphi}(\mathcal{A})\} \in \mathcal{G}, \lambda_A \in \mathbb{R} \text{ such that } \langle \delta\Pi[\boldsymbol{\varphi}, \lambda_A], (\delta\boldsymbol{\varphi}, \delta\lambda_A)\rangle = 0 \; \forall \delta\boldsymbol{\varphi} \in \mathbf{V}^\vartheta, \delta\lambda_A \in \mathbb{R},} \tag{\textbf{MP}}$$

where $\mathbf{V}^\vartheta$ is the set of admissible variations of mappings in $\mathbf{V}$,

$$\Pi[\boldsymbol{\varphi}, \lambda_A] := \Pi_B[\boldsymbol{\varphi}] + \Pi_F[\boldsymbol{\varphi}] + \lambda_A \left(\Pi_A[\boldsymbol{\varphi}] - A_0\right), \tag{7}$$

and the linearization of Π is defined as

$$\langle \delta\Pi[\boldsymbol{\varphi}, \lambda_A], (\delta\boldsymbol{\varphi}, \delta\lambda_A)\rangle := \lim_{\varepsilon \to 0} \frac{d}{d\varepsilon} \Pi[\boldsymbol{\varphi} + \varepsilon\delta\boldsymbol{\varphi}, \lambda_A + \varepsilon\delta\lambda_A]. \tag{8}$$

For brevity, we omit the volume constraint in (**MP**) and in subsequent discussions. The Lagrange multiplier λ_A is introduced to enforce the constraint $\Pi_A = A_0$. Note that we have implicitly replaced the argument Υ of the functionals Π_B, Π_A and Π_F in (2)–(5) by the parameterization $\boldsymbol{\varphi}$ of Υ.

Before proceeding, we emphasize that (**MP**) identifies stationary points without regard for stability. That is, the identified solutions may not be minima (local or global) of the energy functional.

3.2. Restricted set of admissible solutions: offset surfaces

It is appealing to identify the solution Υ of (**MP**) by computing its parameterization $\boldsymbol{\varphi} \in \mathbf{V}$. Nevertheless, it is evident that (**MP**) does not yield a unique choice for $\boldsymbol{\varphi}$ since the functional Π in (7) and the constraint $\Pi_A = A_0$ depend intrinsically on the set Υ. To wit, if $\boldsymbol{\psi} : \mathcal{A} \to \mathcal{A}$ is any smooth automorphism on $\mathcal{A}$, then both $\boldsymbol{\varphi}$ and $\boldsymbol{\varphi} \circ \boldsymbol{\psi}$ are admissible parameterizations for Υ. Consequently, resolving (**MP**) by computing, say, the three Cartesian coordinates for Υ as independent fields over $\mathcal{A}$ results in an ill-posed problem. Instead, we restrict the set of admissible solution surfaces by seeking parameterizations of a specific form, namely, by requiring that admissible solutions be normal offsets of a given surface.

Let $\Upsilon^0 \subset \mathbb{R}^3$ be the surface

$$\Upsilon^0 := \{\boldsymbol{\varphi}^0(\boldsymbol{\xi}) : \boldsymbol{\xi} \in \mathcal{A}, \boldsymbol{\varphi}^0 \in \mathbf{V} \cap [H^3(\mathcal{A})]^3\}. \tag{9}$$

Consider the set

$$\mathcal{G}(\Upsilon^0) := \{\gamma = \{\boldsymbol{\varphi}^0(\boldsymbol{\xi}) + w(\boldsymbol{\xi})\,\mathbf{n}^0(\boldsymbol{\xi}) : \boldsymbol{\xi} \in \mathcal{A}\}, \gamma \subset \mathcal{N}(\Upsilon^0), w \in H^2_0(\mathcal{A})\}, \tag{10}$$

where $\mathbf{n}^0$ is the unit normal to Υ^0 and $\mathcal{N}(\Upsilon^0)$ is the *tubular neighborhood* of Υ^0. As illustrated in Fig. 2, a surface $\gamma \in \mathcal{G}(\Upsilon^0)$ is a *normal perturbation* of Υ^0 and is defined by the parameterization

$$\boldsymbol{\varphi}(\boldsymbol{\xi}) := \boldsymbol{\varphi}^0(\boldsymbol{\xi}) + w(\boldsymbol{\xi})\,\mathbf{n}^0(\boldsymbol{\xi}), \; \boldsymbol{\xi} \in \mathcal{A}. \tag{11}$$

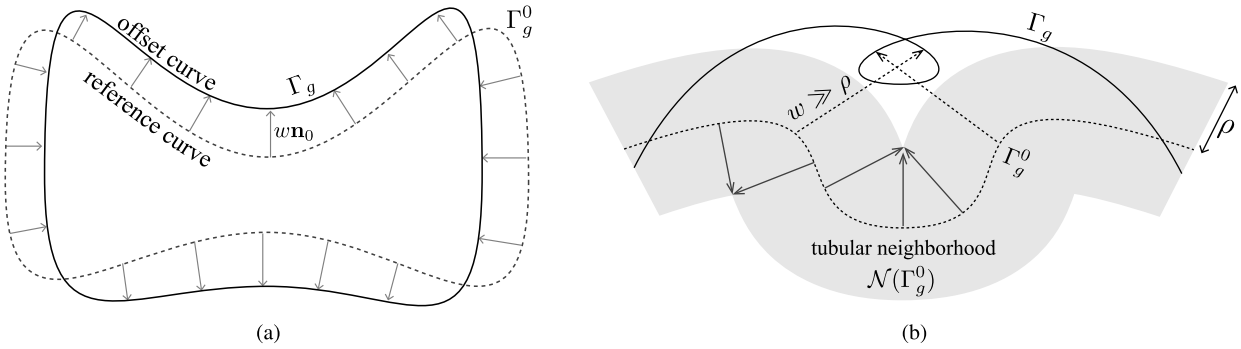

Fig. 3. An offset surface Υ is defined as a normal perturbation of a reference surface Υ^0. For the purpose of visualization, only sections of these surfaces are depicted here. Figure (b) shows that when the normal perturbation w is too large compared to the local curvature of Υ^0, the resulting offset surface is no longer contained in the tubular neighborhood $\mathcal{N}(\Upsilon^0)$ of Υ^0 and may fail to be regular.

For this reason, we say that $\gamma \in \mathcal{G}(\Upsilon^0)$ is a *normal offset* of Υ^0. We refer to Υ^0 as the *reference surface* for γ, and to w as the offset coordinate.

A few remarks are pertinent here.

(i) The higher regularity required of Υ^0 and the conditions $\boldsymbol{\varphi}^0 \in \mathbf{V}$, $w \in H_0^2(\mathcal{A})$ imply that $\mathcal{G}(\Upsilon^0) \subseteq \mathcal{G}$. In general, $\mathcal{G}(\Upsilon^0)$ is strictly contained in $\mathcal{G}$.

(ii) It is possible to identify the surfaces in $\mathcal{G}$ that belong to $\mathcal{G}(\Upsilon^0)$. To this end, let

$$\mathcal{G}_{\mathrm{N}} := \{\gamma \in \mathcal{G} : \gamma \subset \mathcal{N}(\Upsilon^0)\}, \tag{12}$$

which consists of surfaces in $\mathcal{G}$ that lie in the tubular neighborhood of Υ^0. It follows from definitions (10) and (12) that

$$\gamma \in \mathcal{G}(\Upsilon^0) \Rightarrow \gamma \in \mathcal{G}_{\mathrm{N}}. \text{ Hence } \mathcal{G}(\Upsilon^0) \subseteq \mathcal{G}_{\mathrm{N}}. \tag{13}$$

Conversely, suppose that $\gamma \in \mathcal{G}_{\mathrm{N}}$. Using the assumption $\gamma \subset \mathcal{N}(\Upsilon^0)$, we know that for each $\boldsymbol{\xi} \in \mathcal{A}$, there exists a unique scalar $w(\boldsymbol{\xi})$ such that $\boldsymbol{\varphi}^0(\boldsymbol{\xi}) + w(\boldsymbol{\xi})\mathbf{n}^0(\boldsymbol{\xi}) \in \gamma$, see [42, Chapter 2]. Therefore, it follows that

$$\gamma \in \mathcal{G}_{\mathrm{N}} \Rightarrow \gamma \in \mathcal{G}(\Upsilon^0). \text{ Hence } \mathcal{G}_{\mathrm{N}} \subseteq \mathcal{G}(\Upsilon^0). \tag{14}$$

From (13) and (14), we conclude that $\mathcal{G}_{\mathrm{N}} = \mathcal{G}(\Upsilon^0)$.

(iii) The offset coordinate for a surface $\gamma \in \mathcal{G}_{\mathrm{N}}$ as a member of $\mathcal{G}(\Upsilon^0)$ is in fact easy to compute. Denoting the Euclidean distance in $\mathbb{R}^3$ by $d(\cdot,\cdot)$, let

$$\boldsymbol{\xi}^0(\mathbf{x} \in \gamma) = \arg\min_{\zeta \in \mathcal{A}} d(\mathbf{x}, \boldsymbol{\varphi}^0(\zeta)).$$

We understand $\boldsymbol{\xi}^0(\mathbf{x})$ to be the parametric coordinate of the closest point projection of $\mathbf{x}$ onto Υ^0. It is well defined owing to the regularity of Υ^0 and the assumption $\mathbf{x} \in \gamma \subset \mathcal{N}(\Upsilon^0)$, see [42]. Then the offset $W(\mathbf{x})$ at $\mathbf{x} \in \gamma$ is given by

$$W(\mathbf{x} \in \gamma) = \{\mathbf{x} - \boldsymbol{\varphi}^0(\boldsymbol{\xi}^0(\mathbf{x}))\} \cdot \mathbf{n}^0(\boldsymbol{\xi}^0(\mathbf{x})).$$

3.3. Variational formulation restricted to offset surfaces

Given a reference surface Υ^0, we consider the restriction of (**MP**) to surfaces in $\mathcal{G}(\Upsilon^0)$. Admitting the abuse of notation $\Pi[w, \lambda_A] := \Pi[\boldsymbol{\varphi}^0 + w\,\mathbf{n}^0, \lambda_A]$, we have

$$\boxed{\begin{aligned}&\text{Given } \Upsilon^0 = \{\boldsymbol{\varphi}^0(\mathcal{A})\}, \text{ find } (w, \lambda_A) \in H_0^2(\mathcal{A}) \times \mathbb{R} \text{ such that:}\\ &\qquad\qquad \langle \delta\Pi[w, \lambda_A], (\delta w, \delta\lambda_A)\rangle = 0 \;\forall (\delta w, \delta\lambda_A) \in H_0^2(\mathcal{A}) \times \mathbb{R}.\end{aligned}} \tag{**P**}$$

As understood in (**P**), we shall henceforth identify $\Pi_A[w]$ and $\Pi_F[w]$ with $\Pi_A[\boldsymbol{\varphi}^0 + w\,\mathbf{n}^0]$ and $\Pi_F[\boldsymbol{\varphi}^0 + w\,\mathbf{n}^0]$, respectively.

We argued previous in Section 3.2 that each surface in $\mathcal{G}(\Upsilon^0)$ is defined by a unique offset coordinate w in (11). Hence (**P**) is recovered from (**MP**) by restricting the class of admissible solution surfaces to the subset $\mathcal{G}(\Upsilon^0)$ of $\mathcal{G}$. The relation between problems (**MP**) and (**P**) depends crucially on the choice of the reference surface Υ^0. If Υ^0 is chosen such that the solution Υ of (**MP**) is contained in $\mathcal{N}(\Upsilon^0)$, then Υ is a solution of (**P**) as well. This in turn requires that Υ be a sufficiently small perturbation of Υ^0, see Fig. 3. In this sense, we interpret Υ^0 as a reasonable initial guess for the solution of (**MP**). In Section 4.4, we discuss computing solutions that are large perturbations of an initial guess Υ^0 by considering a sequence of incrementally loaded problems and updating the choice of the reference surface at each load step.

3.4. Evaluation of the weak form

We provide detailed expressions to evaluate the weak form (**P**). We provide an intentionally terse description of the necessary geometric preliminaries and refer to [42] for details. Throughout, we shall denote the Cartesian coordinates of $\boldsymbol{\xi} \in \mathbb{R}^2$ by (ξ_1, ξ_2). The scalar and vector products in $\mathbb{R}^3$ are denoted by $(\cdot)$ and $(\times)$, respectively.

3.4.1. Geometric preliminaries

Let $\gamma \in \mathcal{G}(\Upsilon^0)$ be a surface with parameterization

$$\boldsymbol{\varphi}(\boldsymbol{\xi}) = \boldsymbol{\varphi}^0(\boldsymbol{\xi}) + w(\boldsymbol{\xi})\,\mathbf{n}^0(\boldsymbol{\xi}),\ \boldsymbol{\xi} \in \mathcal{A}. \tag{15}$$

The tangent plane to γ at $\boldsymbol{\varphi}(\boldsymbol{\xi})$ is spanned by the basis $\{\mathbf{a}_1, \mathbf{a}_2\}$ defined as

$$\mathbf{a}_\alpha := \boldsymbol{\varphi}_{,\alpha} = \boldsymbol{\varphi}^0_{,\alpha} + w_{,\alpha}\mathbf{n}^0 + w\mathbf{n}^0_{,\alpha},\ \alpha = 1, 2 \tag{16}$$

where $(\cdot)_{,\alpha}$ equals the derivative $\partial(\cdot)/\partial\xi_\alpha$. The unit normal to γ is given by the Gauss map

$$\mathbf{n} = \frac{\mathbf{a}_1 \times \mathbf{a}_2}{\|\mathbf{a}_1 \times \mathbf{a}_2\|}. \tag{17}$$

The components of the metric tensor g and the coefficients of the second fundamental form L in the basis $\{\mathbf{a}_1, \mathbf{a}_2\}$ are given by

$$\mathrm{g}_{\alpha\beta} = \mathbf{a}_\alpha \cdot \mathbf{a}_\beta, \quad \mathrm{L}_{\alpha\beta} = \mathbf{a}_{\alpha,\beta} \cdot \mathbf{n}, \quad 1 \le \alpha, \beta \le 2. \tag{18}$$

To compute the differential of the Gauss map, we use the components of the shape operator S in the $\{\mathbf{a}_1, \mathbf{a}_2\}$ basis

$$\mathbf{n}_{,\alpha} = \sum_{\beta=1}^{2} \mathrm{S}_{\alpha\beta}\mathbf{a}_\beta,\ \text{where } \mathrm{S} := -\mathrm{L}\,\mathrm{g}^{-1}, \tag{19}$$

where g^{-1} is the (matrix) inverse of g. We may now evaluate the area element $\mathrm{J}d\mathcal{A}$ of γ and its mean curvature H as

$$\mathrm{J} = \sqrt{\det(\mathrm{g})}, \quad \mathrm{H} = \frac{1}{2}\mathrm{Tr}(\mathrm{S}), \tag{20}$$

where det and Tr are the (matrix) determinant and trace operators, respectively. Finally, we mention that the components of the differential of the Gauss map $\mathbf{n}^0_{,\alpha}$ of the reference surface Υ^0 appearing in (16) can itself be evaluated using the shape operator of Υ^0.

3.4.2. Expressions for the weak form

Adopting the shorthand $\delta_w(\cdot) := \langle(\cdot), \delta w\rangle$ for an admissible variation δw, the weak form in (**P**) is recast as

$$\langle \delta\Pi[w, \lambda_A], (\delta w, \delta\lambda_A)\rangle = \delta_w\Pi_B[w] + \delta_w\Pi_F[w] + \lambda_A\delta_w\Pi_A[w] + \delta\lambda_A(\Pi_A[w] - A_0). \tag{21}$$

To evaluate the linearizations of functionals Π_B, Π_A and Π_F in (21), we use definitions (2), (3), (5) and (8) to get

$$\delta_w\Pi_B[w] = \delta_w\left(\frac{\kappa_b}{2}\int_{\mathcal{A}} \mathrm{H}^2\,\mathrm{J}\,d\mathcal{A}\right) = \frac{\kappa_b}{2}\int_{\mathcal{A}} \left(2\mathrm{H}\mathrm{J}\,\delta_w\mathrm{H} + \mathrm{H}^2\delta_w\mathrm{J}\right) d\mathcal{A}, \tag{22a}$$

$$\delta_w\Pi_A[w] = \delta_w\left(\int_{\mathcal{A}} \mathrm{J}\,d\mathcal{A}\right) = \int_{\mathcal{A}} \delta_w\mathrm{J}\,d\mathcal{A}, \tag{22b}$$

$$\delta_w\Pi_F[w] = \delta_w\left(\int_{\mathcal{A}} \mu[\boldsymbol{\varphi}]\mathrm{J}d\mathcal{A}\right) = \int_{\mathcal{A}} \left(\frac{\partial\mu}{\partial\boldsymbol{\varphi}}\delta_w\boldsymbol{\varphi}\,\mathrm{J} + \mu\,\delta_w\mathrm{J}\right) d\mathcal{A}. \tag{22c}$$

Linearizations of the geometric quantities appearing in (22) are in turn computed using the following cascade of expressions derived directly from definitions (15)–(20).

$$
\begin{aligned}
\delta_w \boldsymbol{\varphi} &= \delta w\, \mathbf{n}^0, \\
\delta_w \mathbf{a}_\alpha &= \delta w_{,\alpha}\, \mathbf{n}^0 + \delta w\, \mathbf{n}^0_{,\alpha}, \\
\delta_w \mathbf{a}_{\alpha,\beta} &= \delta w\, \mathbf{n}^0_{,\alpha\beta} + \delta w_{,\alpha}\, \mathbf{n}^0_{,\beta} + \delta w_{,\beta}\, \mathbf{n}^0_{,\alpha} + \delta w_{,\alpha\beta}\, \mathbf{n}^0, \\
\delta_w g_{\alpha\beta} &= \delta_w \mathbf{a}_\alpha \cdot \mathbf{a}_\beta + \delta_w \mathbf{a}_\beta \cdot \mathbf{a}_\alpha, \\
\delta_w \mathrm{g}^{-1} &= -\mathrm{g}^{-1}\, \delta_w \mathrm{g}\, \mathrm{g}^{-1}, \\
\delta_w (\mathbf{a}_1 \times \mathbf{a}_2) &= \delta_w \mathbf{a}_1 \times \mathbf{a}_2 + \mathbf{a}_1 \times \delta_w \mathbf{a}_2, \\
\delta_w \mathrm{J} &= \delta_w (\|\mathbf{a}_1 \times \mathbf{a}_2\|) = \delta_w (\mathbf{a}_1 \times \mathbf{a}_2) \cdot \mathbf{n}, \\
\delta_w \mathbf{n} &= \frac{1}{\mathrm{J}} \left(\delta_w (\mathbf{a}_1 \times \mathbf{a}_2) - \delta_w \mathrm{J}\, \mathbf{n} \right), \\
\delta_w \mathrm{L}_{\alpha\beta} &= \delta_w \mathbf{a}_{\alpha,\beta} \cdot \mathbf{n} + \mathbf{a}_{\alpha,\beta} \cdot \delta_w \mathbf{n}, \\
\delta_w \mathrm{S} &= -\delta_w \mathrm{L}\, \mathrm{g}^{-1} - \mathrm{L}\, \delta_w \mathrm{g}^{-1}, \\
\delta_w \mathrm{H} &= \frac{1}{2} \mathrm{Tr}(\delta_w \mathrm{S}).
\end{aligned}
\tag{23}
$$

In (23), we have repeatedly used the linearity of the operator δ_w, the chain rule, and the commutativity of δ_w and Tr. To compute the linearization of g^{-1}, we use

$$
\mathrm{g}\mathrm{g}^{-1} = \text{Identity} \Rightarrow \delta_w (\mathrm{g}\mathrm{g}^{-1}) = 0 \Rightarrow \delta_w \mathrm{g}\, \mathrm{g}^{-1} + \mathrm{g}\, \delta_w \mathrm{g}^{-1} = 0 \Rightarrow \delta_w \mathrm{g}^{-1} = -\mathrm{g}^{-1}\, \delta_w \mathrm{g}\, \mathrm{g}^{-1},
$$

while the expression for $\delta_w \mathbf{n}$ is computed using

$$
\mathrm{J}\mathbf{n} = \mathbf{a}_1 \times \mathbf{a}_2 \;\Rightarrow\; \delta_w \mathrm{J}\, \mathbf{n} + \mathrm{J}\, \delta_w \mathbf{n} = \delta_w (\mathbf{a}_1 \times \mathbf{a}_2) \;\Rightarrow\; \delta_w \mathbf{n} = \frac{1}{\mathrm{J}} \left(\delta_w (\mathbf{a}_1 \times \mathbf{a}_2) - \delta_w \mathrm{J}\, \mathbf{n} \right). \tag{24}
$$

Owing to the structure of the parameterization chosen in (15), it is possible to provide a geometric interpretation for some of the linearizations in (23). For the purpose of numerical computations however, we will not make specific use of such insights and therefore omit their discussion here.

3.5. Linearization of the weak form

The Galerkin discretization of the weak form (**P**) (equivalently (21)) yields a system of nonlinear algebraic equations for the degrees of freedom of the offset coordinate and the Lagrange multiplier. For its resolution using a Newton-type method, we require the linearization of the weak form. We record necessary expressions here.

Analogous to (8), the linearization of $\langle \delta\Pi[w, \lambda_A], (\delta w, \delta\lambda_A) \rangle$ along $(\Delta w, \Delta\lambda_A) \in H^2_0(\mathcal{A}) \times \mathbb{R}$ is given by

$$
\langle \delta^2\Pi[w, \lambda_A], (\delta w, \delta\lambda_A), (\Delta w, \Delta\lambda_A) \rangle := \lim_{\varepsilon \to 0} \frac{d}{d\varepsilon} \langle \delta\Pi[w + \varepsilon \Delta w, \lambda_A + \varepsilon \Delta\lambda_A], (\delta w, \delta\lambda_A) \rangle. \tag{25}
$$

Employing the shorthand $\Delta_w(\cdot) := \langle (\cdot), \Delta w \rangle$, using (21) in (25), and noting that $(\Delta w, \Delta\lambda_A)$ is independent of the variation $(\delta w, \delta\lambda_A)$, we get

$$
\begin{aligned}
&\langle \delta^2\Pi[w, \lambda_A], (\delta w, \delta\lambda_A), (\Delta w, \Delta\lambda_A) \rangle \\
&\quad = \Delta_w(\delta_w \Pi_B[w]) + \Delta_w(\delta_w \Pi_F[w]) + \lambda_A \Delta_w(\delta_w \Pi_A[w]) + \delta\lambda_A(\Delta_w \Pi_A[w]) + \Delta\lambda_A \delta_w \Pi_A[w].
\end{aligned} \tag{26}
$$

The penultimate pair of terms in (26) are readily evaluated using the expressions derived in Section 3.4.2. The remaining terms are evaluated using (22) in definition (25),

$$
\Delta_w(\delta_w \Pi_B[w]) = \kappa_b \int_{\mathcal{A}} \left[(\Delta_w \mathrm{H}\, \delta_w \mathrm{H} + \mathrm{H}\, \Delta_w \delta_w \mathrm{H})\, \mathrm{J} + (\Delta_w \mathrm{J}\, \delta_w \mathrm{H} + \delta_w \mathrm{J}\, \Delta_w \mathrm{H})\, \mathrm{H} + \frac{\mathrm{H}^2}{2} \Delta_w(\delta_w \mathrm{J}) \right] d\mathcal{A}, \tag{27a}
$$

$$
\Delta_w(\delta_w \Pi_A[w]) = \int_{\mathcal{A}} \Delta_w(\delta_w \mathrm{J})\, d\mathcal{A}, \tag{27b}
$$

$$
\Delta_w(\delta_w \Pi_F[w]) = \int_{\mathcal{A}} \left[\Delta_w \boldsymbol{\varphi}\, \frac{\partial^2 \mu}{\partial \boldsymbol{\varphi}^2} \delta_w \boldsymbol{\varphi}\, \mathrm{J} + \frac{\partial \mu}{\partial \boldsymbol{\varphi}} (\delta_w \boldsymbol{\varphi}\, \Delta_w \mathrm{J} + \Delta_w \boldsymbol{\varphi}\, \delta_w \mathrm{J}) \right] d\mathcal{A}. \tag{27c}
$$

In (27c), we have used the independence of variations δw and Δw to infer $\Delta_w(\delta_w \boldsymbol{\varphi}) = \Delta_w(\delta_w w)\, \mathbf{n}^0 = 0$. The same reasoning also reveals that $\Delta_w(\delta_w \mathbf{a}_\alpha) = \Delta_w(\delta_w \mathbf{a}_{\alpha,\beta}) = 0$ for each $1 \le \alpha, \beta \le 2$.

To evaluate (27) and in turn (26), it remains to compute the second variations $\Delta_w(\delta_w\boldsymbol{\varphi})$, $\Delta_w(\delta_w \mathrm{J})$ and $\Delta_w(\delta_w \mathrm{H})$ appearing in (27). From definitions (15)–(20) and their linearizations (23), we have

$$\boxed{\begin{aligned}
\Delta_w\delta_w \mathrm{g}_{\alpha\beta} &= \delta_w\mathbf{a}_\alpha\cdot\Delta_w\mathbf{a}_\beta + \Delta_w\mathbf{a}_\alpha\cdot\delta_w\mathbf{a}_\beta,\\
\Delta_w\delta_w(\mathrm{g}^{-1}) &= -\left(\Delta_w\mathrm{g}^{-1}\,\delta_w\mathrm{g}\,\mathrm{g}^{-1} + \mathrm{g}^{-1}\,\Delta_w\delta_w\mathrm{g}\,\mathrm{g}^{-1} + \mathrm{g}^{-1}\delta_w\mathrm{g}\,\Delta_w\mathrm{g}^{-1}\right),\\
\Delta_w\delta_w(\mathbf{a}_1\times\mathbf{a}_2) &= \delta_w\mathbf{a}_1\times\Delta_w\mathbf{a}_2 + \Delta_w\mathbf{a}_1\times\delta_w\mathbf{a}_2,\\
\Delta_w\delta_w \mathrm{J} &= \Delta_w\delta_w(\mathbf{a}_1\times\mathbf{a}_2)\cdot\mathbf{n} + \delta_w(\mathbf{a}_1\times\mathbf{a}_2)\cdot\Delta_w\mathbf{n},\\
\Delta_w\delta_w\mathbf{n} &= \frac{1}{\mathrm{J}}\left(\Delta_w\delta_w(\mathbf{a}_1\times\mathbf{a}_2) - \Delta_w\delta_w\mathrm{J}\,\mathbf{n} - \delta_w\mathrm{J}\Delta_w\mathbf{n} - \Delta_w\mathrm{J}\delta_w\mathbf{n}\right),\\
\Delta_w\delta_w \mathrm{L}_{\alpha\beta} &= \delta_w\mathbf{a}_{\alpha,\beta}\cdot\Delta_w\mathbf{n} + \Delta_w\mathbf{a}_{\alpha,\beta}\cdot\delta_w\mathbf{n} + \mathbf{a}_{\alpha,\beta}\cdot\Delta_w\delta_w\mathbf{n},\\
\Delta_w\delta_w \mathrm{S} &= -\left(\Delta_w\delta_w\mathrm{L}\,\mathrm{g}^{-1} + \mathrm{L}\Delta_w\delta_w\mathrm{g}^{-1} + \delta_w\mathrm{L}\,\Delta_w\mathrm{g}^{-1} + \Delta_w\mathrm{L}\,\delta_w\mathrm{g}^{-1}\right),\\
\Delta_w\delta_w \mathrm{H} &= \frac{1}{2}\mathrm{Tr}\left(\Delta_w\delta_w\mathrm{S}\right).
\end{aligned}} \tag{28}$$

To compute $\Delta_w\delta_w\mathbf{n}$ in (28), we use a calculation similar to (24),

$$\mathbf{a}_1\times\mathbf{a}_2 = \mathrm{J}\mathbf{n} \;\Rightarrow\; \Delta_w\delta_w(\mathbf{a}_1\times\mathbf{a}_2) = \Delta_w\delta_w\mathrm{J}\,\mathbf{n} + \mathrm{J}\,\Delta_w\delta_w\mathbf{n} + \delta_w\mathrm{J}\,\Delta_w\mathbf{n} + \Delta_w\mathrm{J}\,\delta_w\mathbf{n}. \tag{29}$$

4. Galerkin finite element approximation

Let $V\subset H^2_0(\mathcal{A})$ be a finite dimensional subspace (the finite element space). A Galerkin approximation of (**P**) is the problem:

$$\boxed{\begin{aligned}&\text{Given } \Upsilon^0 = \{\boldsymbol{\varphi}^0(\mathcal{A})\},\ \text{find } (w_h,\lambda_h)\in V\times\mathbb{R} \text{ such that:}\\ &\qquad\qquad \langle\delta\Pi[w_h,\lambda_h],(\delta w_h,\delta\lambda_A)\rangle = 0 \quad \forall(\delta w_h,\delta\lambda_h)\in V^\partial\times\mathbb{R},\end{aligned}} \tag{**G**}$$

where V^∂ is the space of admissible variations of functions in V. Without loss of generality, let $V=\mathrm{Span}\{N_a:\mathcal{A}\to\mathbb{R},\ 1\le a\le n\}$ and $\dim(V)=n$. Problem (**G**) is a system of $n+1$ nonlinear algebraic equations of the form

$$\mathbf{R}[w_h,\lambda_h] := \begin{bmatrix}\mathbf{F}[w_h]+\mathbf{f}[w_h]+\lambda_h\mathbf{G}[w_h]\\ \Pi_A[w_h]-A_0\end{bmatrix} = 0. \tag{30}$$

The $n+1$ unknowns in (30) are the n degrees of freedom dual to the basis $\{N_a\}_a$ for V, and the Lagrange multiplier λ_h. The residual $\mathbf{R}$ is an $(n+1)\times 1$ column vector, while the $n\times 1$ column vectors $\mathbf{F}$, $\mathbf{f}$ and $\mathbf{G}$ have components

$$\mathbf{F}_a[w_h] := \langle\delta\Pi_B[w_h],N_a\rangle, \tag{31a}$$

$$\mathbf{f}_a[w_h] := \langle\delta\Pi_F[w_h],N_a\rangle, \tag{31b}$$

$$\mathbf{G}_a[w_h] := \langle\delta\Pi_A[w_h],N_a\rangle, \quad 1\le a\le n. \tag{31c}$$

The arguments w_h and λ_h in (30) and (31) explicitly denote dependence on w_h and λ_h. That (30) is a realization of (**G**) for a specific choice of variations is evident from

$$\mathbf{R}_a[w_h,\lambda_h] = \begin{cases}\langle\delta\Pi[w_h],(N_a,0)\rangle & \text{for } 1\le a\le n,\\ \langle\delta\Pi[w_h],(0,1)\rangle & \text{for } a=n+1.\end{cases} \tag{32}$$

The splitting of terms in (30) is a chosen to closely reflect (21). At a given (admissible) solution guess (w_h,λ_h), $\mathbf{R}$ is evaluated using the expressions derived in (22) for each of the terms in (31).

To compute (w_h,λ_h) satisfying (30), we resort to a Newton method. Let $\mathbf{K}[w_h]$, $\mathbf{L}[w_h]$ and $\mathbf{M}[w_h]$ be the $n\times n$ matrices with components

$$\mathbf{K}_{ab}[w_h] := \langle\delta^2\Pi_B[w_h],N_a,N_b\rangle, \tag{33a}$$

$$\mathbf{L}_{ab}[w_h] := \langle\delta^2\Pi_F[w_h],N_a,N_b\rangle, \tag{33b}$$

$$\mathbf{M}_{ab}[w_h] := \langle\delta^2\Pi_A[w_h],N_a,N_b\rangle, \quad 1\le a,b\le n, \tag{33c}$$

which are the consistent linearizations of $\mathbf{F}$, $\mathbf{f}$ and $\mathbf{G}$, respectively. The matrices $\mathbf{K}$, $\mathbf{L}$ and $\mathbf{M}$ are evaluated using the choice of variations indicated in (33) and the expressions in (27). The argument w_h in (33) again highlights the fact that the tangent matrices are configuration dependent, which is a consequence of the nonlinearity of the problem. A Newton method to solve (30) consists in the iterative two-step procedure

$$\text{Solve:} \quad \mathbf{A}[w_h, \lambda_h] \begin{bmatrix} \Delta \mathbf{w} \\ \Delta \lambda \end{bmatrix} = \mathbf{R}[w_h, \lambda_h], \tag{34a}$$

$$\text{Update:} \quad (w_h, \lambda_h) \leftarrow (w_h, \lambda_h) - (\Delta w_h, \Delta \lambda), \tag{34b}$$

$$\text{where } \Delta w_h = \sum_{a=1}^{n} \Delta \mathbf{w}_a N_a \text{ and } \mathbf{A}[w_h, \lambda_h] = \begin{bmatrix} \mathbf{K}[w_h] + \mathbf{L}[w_h] + \lambda_h \mathbf{M}[w_h] & \mathbf{G}[w_h] \\ \mathbf{G}[w_h]^{\mathrm{T}} & 0 \end{bmatrix}. \tag{34c}$$

The $(n+1) \times (n+1)$ matrix $\mathbf{A}$ is the linearization of the residual $\mathbf{R}$. Observe that the definition of $\mathbf{A}$ in (34c) is a realization of (26) for a specific choices of variations $(\delta w, \delta \lambda_A)$ and $(\Delta w, \Delta \lambda_A)$, namely,

$$\mathbf{A}_{ab}[w_h, \lambda_h] = \begin{cases} \langle \delta^2 \Pi[w_h, \lambda_h], (N_a, 0), (N_b, 0) \rangle & \text{for } 1 \le a, b \le n, \\ \langle \delta^2 \Pi[w_h, \lambda_h], (N_a, 0), (0, 1) \rangle & \text{for } 1 \le a \le n, b = n+1, \\ \langle \delta^2 \Pi[w_h, \lambda_h], (0, 1), (N_b, 0) \rangle & \text{for } a = n+1, 1 \le b \le n, \\ \langle \delta^2 \Pi[w_h, \lambda_h], (0, 1), (0, 1) \rangle & \text{for } a = b = n+1. \end{cases} \tag{35}$$

Algorithm 1 below summarizes the steps to solve (30) to compute w_h and λ_h. Therein, we implicitly assume that the given reference surface Υ^0 is maintained fixed across Newton iterations. It is indeed possible, and sometimes necessary, to update the choice of Υ^0 either periodically, or at the end of each iteration. Such updates are incorporated in Algorithm 2. The simple two-step strategy in (34) is used for solution updates and in all our numerical examples. It can be substituted with more sophisticated line search methods [44]. For simplicity, we take the initial guesses for w_h and λ_h to be zero. As indicated in the algorithm as well as in all our simulations, we choose the ℓ^2-norm for checking convergence of the residual.

4.1. Spline-based finite elements

The regularity requirement $w \in H_0^2(\mathcal{A})$ in (**P**) stems from the dependence of the bending energy on the mean curvature. This in turn necessitates constructing finite dimensional subspaces of $H_0^2(\mathcal{A})$ in problem (**G**). Requiring a continuously differentiable interpolation for the normal offset immediately precludes the possibility of using piecewise polynomial Lagrange interpolations for w_h in (**G**). It is possible to use mixed finite element methods employing independent interpolations for w_h and its derivatives, see [16,25,26]. Instead, we adopt tensor-product b-spline functions for this purpose and assume for simplicity that $\mathcal{A} = \mathrm{I} \times \mathrm{I}$, where $\mathrm{I} := [0, 1]$. First we recall a few essential facts about one-dimensional B-splines.

4.1.1. B-spline functions

Let $p \ge 0$ be an integer and T be the knot vector

$$\mathrm{T} = \{t_{-p} < t_{-p+1} < \ldots < 0 = t_0 < t_1 < \ldots < t_m = 1 < t_{m+1} < \ldots < t_{m+p}\}, \tag{36}$$

consisting of an increasing sequence of real numbers. The knot spacing $h := \max_{i=-p}^{m+p-1} (t_{i+1} - t_i)$ denotes the maximum length of an interval in T. The ith b-spline function of degree p is denoted by $N_{i,p}$ and is defined by the recursive relation

$$N_{i,0}(t) = \begin{cases} 1 & \text{if } t_i \le t \le t_{i+1}, \\ 0 & \text{otherwise,} \end{cases} \quad \text{and} \tag{37a}$$

$$N_{i,p}(t) = \frac{t - t_i}{t_{i+1} - t_i} N_{i,p-1}(t) + \frac{t_{i+p+1} - t}{t_{i+p+1} - t_{i+1}} N_{i+1,p-1}(t), \tag{37b}$$

where $i = 0$ to $m + p - 1$; see Fig. 4. Efficient algorithms to evaluate b-spline functions and their derivatives have been devised and implemented in commonly used software libraries [45].

The choice of degree p and knot vector T define the finite dimensional space of functions

$$\mathbb{B}_{\mathrm{T},p} := \mathrm{Span}\{N_{i,p} : \mathrm{I} \to \mathbb{R}\}_{i=0}^{m+p-1}. \tag{38}$$

Of particular significance for using b-spline functions as finite element basis functions are the observations that for each $i = 0$ to $m + p - 1$:

- **P1.** $N_{i,p}$ is a piecewise polynomial of degree p. In particular, $\{N_{i,0}\}_i$ are piecewise constants while $\{N_{i,1}\}_i$ are the familiar piecewise linear hat functions.
- **P2.** $N_{i,p}$ is compactly supported in the interval $[t_{i+1-p}, t_{i+1}]$. Consequently, there are at most $p+1$ non-zero basis functions in the interval $[t_i, t_{i+1}]$.
- **P3.** B-spline functions are non-negative and form a partition of unity, i.e., $N_{i,p}(t) \ge 0$ and $\sum_i N_{i,p}(t) = 1$ for any $t \in \mathrm{I}$.
- **P4.** The function $N_{i,p}$ is $p - k$ times differentiable at a knot having multiplicity k, and is smooth elsewhere.
- **P5.** The vector space $\mathbb{B}_{\mathrm{T},p}$ has dimension $m + p$.

Algorithm 1: Solution with given reference surface

Input: Reference surface Υ^0
Input: Tolerance ε for convergence
Initial guess: $(w_h, \lambda_h) \leftarrow 0$
converged $\leftarrow$ false
while *converged* = *false* **do**
  Assemble residual vector $\mathbf{R} := \mathbf{R}[w_h, \lambda_h]$
  if $\|\mathbf{R}\|_{\ell^2} < \varepsilon$ **then**
    converged $\leftarrow$ *true*
  else
    Assemble tangent operator $\mathbf{A} := \mathbf{A}[w_h, \lambda_h]$
    Solve: $\mathbf{A}[\ \Delta\mathbf{w} \quad \Delta\lambda_h\ ]^{\mathrm{T}} = \mathbf{R}$
    Update solution: $(w_h, \lambda_h) \leftarrow (w_h, \lambda_h) - (\Delta w_h, \Delta\lambda_h)$, where $\Delta w_h = \sum_a \Delta\mathbf{w}_a N_a$.
  end
end
return (w_h, λ_h)

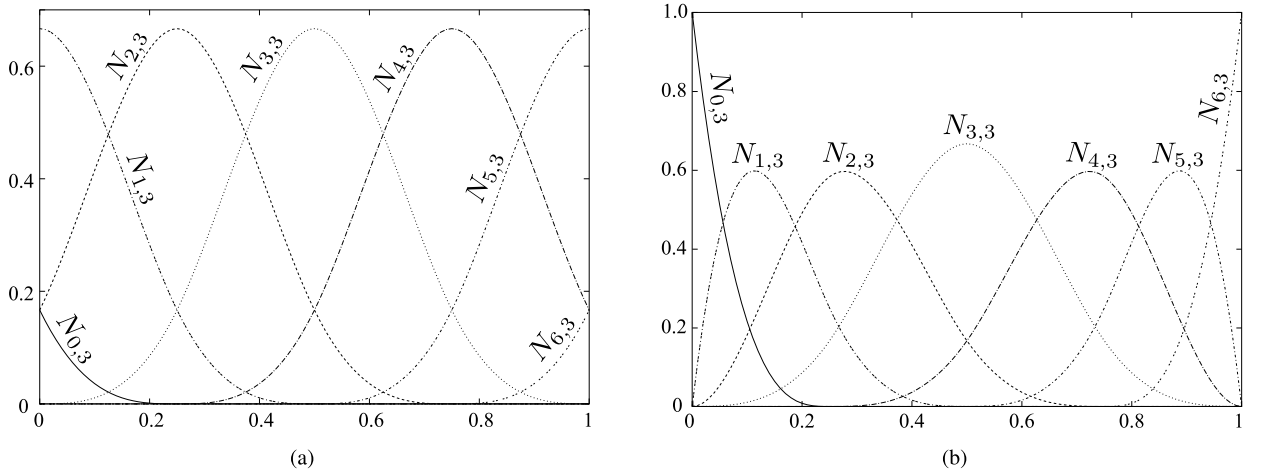

Fig. 4. Plots (a) and (b) show cubic b-spline basis functions defined using knot vectors $\{-0.6, -0.4, -0.2, 0, 0.2, 0.4, 0.6, 0.8, 1, 1.2, 1.4, 1.6\}$ and $\{0, 0, 0, 0, 0.2, 0.4, 0.6, 0.8, 1, 1, 1, 1\}$, respectively. Observe that basis functions are non-negative and sum to 1 at each point. Unlike (a), repeated knots in (b) result in $N_{0,3}(0) = 1$ and $N_{6,3}(1) = 1$, which is useful when imposing Dirichlet boundary conditions.

Property **P**4 reflects the principal advantage of b-splines over Lagrange polynomials in problem (**G**). B-spline functions with high order continuity are achieved by merely increasing the degree p. Choosing $p \geq 2$ ensures that $\mathbb{B}_{\mathrm{T},p} \subset C^1(\mathrm{I})$, which should be compared to C^0 continuity possible with Lagrange basis functions. Besides **P**1–**P**5, b-splines have excellent approximation properties [46]. We note that one-dimensional basis functions with C^1 continuity can also be defined using Hermite polynomials, but their construction is necessarily more tedious.

4.1.2. B-splines as finite element basis functions

B-spline functions facilitate a natural construction of finite element subspaces of $H^2_0(\mathcal{A})$, especially since we have assumed a rectangular parametric domain $\mathcal{A} = \mathrm{I} \times \mathrm{I}$. Let T be as in (36) and let

$$\mathrm{S} := \{s_{-p} < s_{-p+1} < \cdots < 0 = s_0 < s_1 < \cdots < s_n = 1 < s_{n+1} < \cdots < s_{n+p}\}. \tag{39}$$

For each $0 \leq i \leq m-1$ and $0 \leq j \leq n-1$, define the finite element E_{ij} as the 3-tuple [47]

$$\mathrm{E}_{ij} := \Big([t_i, t_{i+1}] \times [s_j, s_{j+1}],\ \mathrm{Span}\{N_{k,p}(x) N_{\ell,p}(y) : i \leq k \leq i+p,\ j \leq \ell \leq j+p\},$$
$$\{\sigma_{k\ell} : i \leq k \leq i+p,\ j \leq \ell \leq \ell+p\} \Big), \tag{40}$$

consisting of an element geometry (a rectangle), the basis functions spanning $V := \mathbb{B}_{\mathrm{T},p} \otimes \mathbb{B}_{\mathrm{S},p}$, and the corresponding set of degrees of freedom. The degrees of freedom $\{\sigma_{k\ell} : 0 \leq k \leq m+p-1, 0 \leq \ell \leq n+p-1\}$ span the dual of V and are defined by the relation

$$f \in V \Rightarrow f(x, y) = \sum_{i=0}^{m+p-1} \sum_{j=0}^{n+p-1} \sigma_{ij}(f) N_{i,p}(x) N_{j,p}(y),\ x, y \in \mathrm{I}. \tag{41}$$

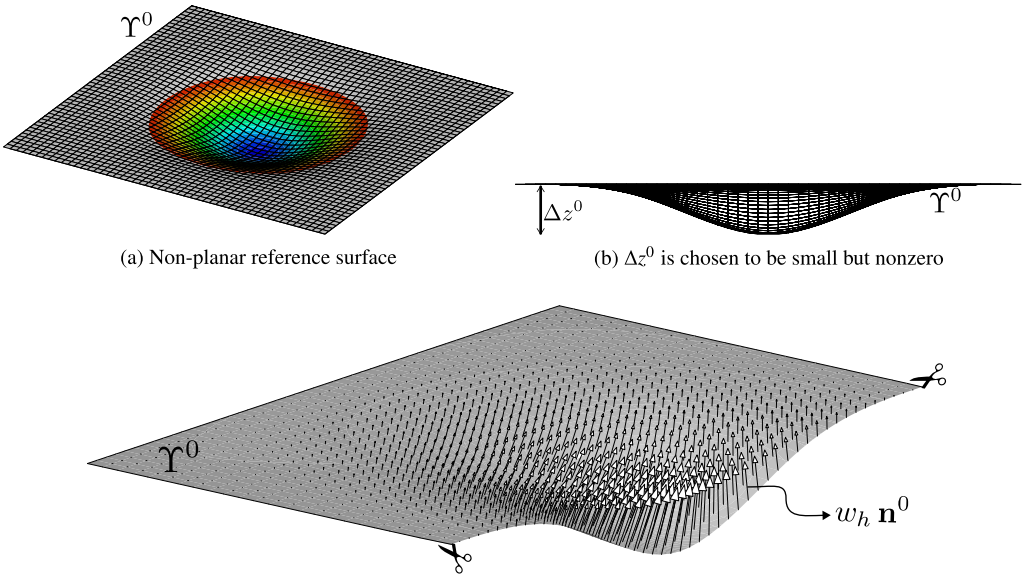

(a) Non-planar reference surface

(b) Δz^0 is chosen to be small but nonzero

(c) Computed finite element solution w_h using quadratic b-spline functions

Fig. 5. Finite element approximation of a planar fluid membrane using a non-planar reference surface.

Notice that we have used the same degree p in the definition of tensor product space V. It is certainly possible, perhaps motivated by features of the solution, to construct V as a tensor product of b-spline function spaces of distinct degrees p and p', i.e., as $\mathbb{B}_{\mathrm{T},p} \otimes \mathbb{B}_{\mathrm{S},p'}$. Nevertheless, all our numerical examples are computed using $p = p'$.

An important distinction between finite elements defined using b-splines in (40) and Lagrange-type elements lies in the interpretation of the degrees of freedom. In the latter, degrees of freedom conveniently coincide with function values at a specific set of points (nodes). This is no longer the case with (40), which is a consequence of the fact that b-spline functions are in general non-interpolatory. Alternately, we may think of $\{\sigma_{ij}(f)\}$ as a set of generalized coordinates for $f \in V$ rather than as a set of nodal values. Consequently, boundary conditions on functions and their derivatives are imposed as linear constraints. In Fig. 4(b), we illustrate the possibility of recovering interpolatory b-spline functions by repeating knot vectors. This is a convenient feature when imposing boundary conditions.

4.2. An illustrative example

We present an example to demonstrate using Algorithm 1 to solve problem (**MP**). For simplicity, we assume that there are no external interactions ($\Pi_F = 0$) and neglect area/volume constraints ($\lambda_A = \lambda_V = 0$). With the standard Cartesian coordinate system $\{\mathbf{e}_1, \mathbf{e}_2, \mathbf{e}_3\}$ for $\mathbb{R}^3$, we consider boundary conditions

$$\begin{cases} \boldsymbol{\varphi} \cdot \mathbf{e}_x = \xi_1 & \text{on } \xi_1 = 0, 1 \\ \boldsymbol{\varphi} \cdot \mathbf{e}_y = \xi_2 & \text{on } \xi_2 = 0, 1 \\ \boldsymbol{\varphi} \cdot \mathbf{e}_z = \partial(\boldsymbol{\varphi} \cdot \mathbf{e}_z)/\partial \mathbf{n} = 0 & \text{on } \partial\mathcal{A}. \end{cases} \tag{42}$$

The solution of (**MP**) satisfying (42) is the planar surface $\Upsilon = \mathcal{A} \times \{0\}$. In fact, since Υ has zero mean curvature, it achieves the minimum bending energy $\Pi_B[\Upsilon] = 0$.

To define the restriction (**P**) of (**MP**), we choose the reference surface Υ^0 depicted in Figs. 5(a) and 5(b). We construct it as a tensor-product cubic b-spline surface parameterized over $\mathcal{A}$ with $7 \times 7 = 49$ control points. Hence

$$\boldsymbol{\varphi}^0(\boldsymbol{\xi}) := \sum_{0 \le i,j \le 6} \mathbf{p}^0_{ij} N_{i,3}(\xi_1) N_{j,3}(\xi_2), \text{ where } \mathbf{p}^0_{ij} \in \mathbb{R}^3, \boldsymbol{\xi} \in \mathcal{A}.$$

The control points $\{\mathbf{p}^0_{ij}\}_{i,j}$ are chosen such that $\boldsymbol{\varphi}^0$ satisfies boundary conditions (42) and Υ^0 is non-planar. The latter choice is intentional, so that we can examine the performance of Algorithm 1 for a problem in which the exact solution is known. The exact solution for the offset coordinate is given by

$$w = \left(\frac{\boldsymbol{\varphi}^0 \cdot \mathbf{e}_z}{\mathbf{n}^0 \cdot \mathbf{e}_z} \right) \mathbf{n}^0 \text{ on } \mathcal{A}, \tag{43}$$

which is well defined since $\mathbf{n}^0 \cdot \mathbf{e}_z > 0$ on $\mathcal{A}$ by choice of Υ^0. Additionally, the choice of control points $\{\mathbf{p}^0_{ij}\}_{i,j}$ is such that the maximum curvature of Υ^0 is sufficiently small. This is ensured by controlling the parameter Δz^0 indicated in Fig. 5(b). As a result, we have $\Upsilon \in \mathcal{N}(\Upsilon^0)$.

Table 1
In (a), we show (approximately quadratic) convergence of the residual with the number of Newton iterations for the simulation depicted in Fig. 5. In (b), we report the number of Newton iterations required to achieve $\|\mathbf{R}\| < 10^{-10}$, the bending energy of the finite element solution, and the $L^2(\mathcal{A})$-norm of the error as the knot vector is refined.

Iteration	$\|\mathbf{R}\|_{\ell^2}$
1	6.014×10^{0}
2	4.990×10^{0}
3	1.224×10^{-1}
4	1.223×10^{-2}
5	1.403×10^{-6}
6	2.744×10^{-14}

(a)

# knots	# Iterations	Energy $\Pi_B[w_h]$	$\|w - w_h\|_{L^2(\mathcal{A})}$
5×5	7	8.999×10^{-2}	4.271×10^{-3}
10×10	6	2.147×10^{-2}	8.205×10^{-4}
20×20	6	6.1×10^{-3}	2.382×10^{-4}
40×40	7	1.511×10^{-3}	6.033×10^{-5}
80×80	7	3.769×10^{-4}	1.513×10^{-5}

(b)

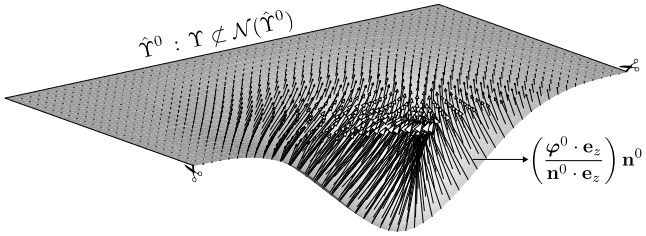

Fig. 6. Since the curvature of the reference surface $\hat{\Upsilon}^0$ is too large, the exact solution does not lie in its tubular neighborhood. This is evident from intersections (non-injectivity) observed in the vector field $w\mathbf{n}^0$.

Fig. 5(c) depicts the Galerkin approximation for the offset coordinate computed using quadratic b-spline functions ($p = 2$) with knot vectors $\mathrm{T} = \mathrm{S}$ and $n = m = 10$ uniformly spaced knots, and satisfies boundary conditions $w_h = \partial w_h / \partial \mathbf{n} = 0$ on $\partial\mathcal{A}$. Since the exact solution w in (43) does not belong to the finite element space $V = \mathbb{B}_{\mathrm{T},2} \otimes \mathbb{B}_{\mathrm{T},2}$, the computed field w_h is only an approximation of w. The ℓ^2-norm of the residual $\mathbf{R}$ as a function of the number of Newton iterations for this calculation is recorded in Table 1(a). We observe that the residual converges approximately quadratically. Table 1(b) reports the number of Newton iterations required to achieve $\|\mathbf{R}\|_{\ell^2} < 10^{-10}$ as a function of the number of knots n (analogous to mesh refinement). We observe that Newton iterations consistently converge in fewer than 7 iterations. We also find that the bending energy of the computed solution and the $L^2(\mathcal{A})$-norm of the error $(w - w_h)$ converge to zero with refinement of the knot vector.

We conclude this example with a remark on the choice of the reference surface. The choice of Υ^0 in Fig. 5 ensures that the exact solution lies in $\mathcal{N}(\Upsilon^0)$. Fig. 6 illustrates the consequence of choosing the reference surface $\hat{\Upsilon}^0$ for which $\Upsilon \not\subset \mathcal{N}(\hat{\Upsilon}^0)$. The surfaces $\hat{\Upsilon}^0$ and Υ^0 identical except that the parameter Δz^0 for $\hat{\Upsilon}^0$ is twice that of Υ^0. Consequently, $\hat{\Upsilon}^0$ has a larger curvature and a correspondingly smaller radius for its tubular neighborhood. Then, as depicted in Fig. 6, the exact solution $\mathcal{A} \times \{0\}$ cannot be reproduced as a regular surface while using an offset parameterization. In numerical experiments, we found that Newton iterations failed to converge with reference surface $\hat{\Upsilon}^0$. However, we caution that non-convergence of Newton iterations is not a reliable indicator of a bad choice for the reference surface.

4.3. B-spline reference surfaces

In principle, the reference surface Υ^0 can be specified in any parametric form that satisfies (9). Nevertheless, it is desirable to devise a systematic construction for them, based on the expected features of the solution so that w_h has both small magnitude as well as small gradients.

As done in the previous example, we construct reference surfaces as tensor-product b-spline surfaces specified by (i) a degree $q \geq 3$, (ii) a pair of knot vectors $\mathrm{T}^0 := \{t_{-q}, \ldots, t_{m'+q}\}$, $\mathrm{S}^0 := \{s_{-q}, \ldots, s_{n'+q}\}$, and (iii) a set of control points $\{\mathbf{p}^0_{ab} \in \mathbb{R}^3 : 0 \leq a \leq m' + q - 1, 0 \leq b \leq n' + q - 1\}$. Hence Υ^0 is the surface with parameterization

$$\boldsymbol{\varphi}^0(\boldsymbol{\xi}) := \sum_{a=0}^{m'+q-1} \sum_{b=0}^{n'+q-1} \mathbf{p}^0_{ab} N_{a,q}(\xi_1) N_{b,q}(\xi_2), \ \boldsymbol{\xi} \in \mathcal{A}. \tag{44}$$

Control points $\{\mathbf{p}^0_{ab}\}_{a,b}$ are chosen to satisfy boundary conditions prescribed for the solution. Choosing the degree $q \geq 3$ ensures that $\boldsymbol{\varphi}^0 \in [H^3(\mathcal{A})]^3$. The degree and knot vectors for Υ^0 can be chosen independently of those defining the finite element space V. A judicious choice $q = p + 1$ is suggested by (11), so that w_h and $\mathbf{n}^0$ have comparable smoothness.

4.4. Incremental solutions

Constructing reference surfaces as b-spline surfaces serves a useful role when studying a one-parameter family of problems $\{\mathbf{P}_\ell\}_\ell$, where each problem $\mathbf{P}_\ell$ is of the form (P). The parameter ℓ may denote, for instance, the evolution of external

Algorithm 2: Incremental solution algorithm

Input: B-spline reference surface Υ_0^0 as $\boldsymbol{\varphi}_0^0(\boldsymbol{\xi}) = \sum_{\substack{0\le a\le n'+q-1\\ 0\le b\le m'+q-1}} \mathbf{p}_{ab}^0 N_{a,q}(\xi_1) N_{b,q}(\xi_2)$

Input: Tolerance ε for convergence

Input: Load increment $\Delta\ell$ and maximum load L

for $\ell = 0$ **to** L **do**

Compute solution at load ℓ: $(w_h, \lambda_h) \leftarrow$ Algorithm 1$(\Upsilon_\ell^0, \varepsilon)$

Compute control points for reference surface $\Upsilon_{\ell+\Delta\ell}^0$ (with bcs):

$$\{\tilde{\mathbf{p}}_{ab}^0\}_{a,b} := \arg\min_{\{\mathbf{q}_{ab}\}_{a,b}} \left\| \sum_{\substack{0\le a\le n'+q-1\\ 0\le b\le m'+q-1}} \mathbf{q}_{ab} N_{a,q}(\xi_1) N_{b,q}(\xi_2) - \boldsymbol{\varphi}_\ell^0(\boldsymbol{\xi}) - w_h(\boldsymbol{\xi})\mathbf{n}^0(\boldsymbol{\xi}) \right\|_{L^2(\mathcal{A})}$$

Define new reference surface $\Upsilon_{\ell+\Delta\ell}^0$: $\boldsymbol{\varphi}_{\ell+\Delta\ell}^0(\boldsymbol{\xi}) = \sum_{\substack{0\le a\le n'+q-1\\ 0\le b\le m'+q-1}} \tilde{\mathbf{p}}_{ab}^0 N_{a,q}(\xi_1) N_{b,q}(\xi_2)$

Increment load: $\ell \leftarrow \ell + \Delta\ell$

end

return Υ_L

loadings, prescribed boundary conditions or imposed constraints. Roughly speaking, we anticipate that the reference surface Υ^0 chosen to compute the solution of $\mathbf{P}_{\ell=0}$ will be unsuitable for computing the solution Υ_ℓ of $\mathbf{P}_\ell$ for any sufficiently large ℓ, because solutions may develop new features with increasing ℓ. Hence we expect that $\Upsilon_\ell \not\subset \mathcal{N}(\Upsilon^0)$ for any sufficiently large parameter ℓ.

Instead, we compute $\{\Upsilon_\ell\}_\ell$ using a corresponding family of reference surfaces $\{\Upsilon_\ell^0\}_\ell$. We assume that the solution Υ_ℓ of $\mathbf{P}_\ell$, as a set in $\mathbb{R}^3$, depends continuously on the parameter ℓ. Hence, the set $\Upsilon_{\ell+\Delta\ell}$ is expected to be close to Υ_ℓ (in the Hausdorff distance, for instance) whenever the load increment $\Delta\ell$ is sufficiently small. Then, we compute $\Upsilon_{\ell+\Delta\ell}$ using the reference surface $\Upsilon_{\ell+\Delta\ell}^0$, which is defined to be a b-spline surface that approximates the known solution Υ_ℓ. Algorithm 2 details such a modification of Algorithm 1, by updating the reference surface at each load increment.

Fig. 7 explains the idea behind Algorithm 2 using the example of an initially flat circular fluid membrane wrapping around a rigid ellipsoidal particle. The details of the external loading used to model adhesion between the membrane and the particle are discussed in Section 6.3. For the current discussion, we shall think of the loading parameter ℓ as the adhesion energy— a larger value for ℓ corresponds to a stronger adhesive interaction between the membrane and the particle, with $\ell = 0$ denoting no adhesion at all. For simplicity, we neglect volume/area constraints. We also use polar coordinates $\boldsymbol{\xi} = (\xi_1 = r, \xi_2 = \theta) \in \mathcal{A} = [0,1] \times [0, 2\pi]$ instead of Cartesian coordinates. Each reference surface $\Upsilon_\ell^0 = \{\boldsymbol{\varphi}_\ell^0(\mathcal{A})\}$ satisfies boundary conditions

$$\begin{aligned} \boldsymbol{\varphi}_\ell^0 \cdot \mathbf{e}_1 = \boldsymbol{\varphi}_\ell^0 \cdot \mathbf{e}_2 = 0, \ \text{at } r = 0, \\ \left(\boldsymbol{\varphi}_\ell^0 \cdot \mathbf{e}_1\right)^2 + \left(\boldsymbol{\varphi}_\ell^0 \cdot \mathbf{e}_2\right)^2 = 1, \ \text{at } r = 1, \\ \frac{\partial \boldsymbol{\varphi}_\ell^0}{\partial r} \cdot \mathbf{e}_3 = \frac{\partial \boldsymbol{\varphi}_\ell^0}{\partial r} \cdot \mathbf{e}_3 = 0, \ \text{at } r = 0, 1, \end{aligned} \tag{45}$$

while the offset coordinate satisfies

$$w_h\Big|_{(r=0,\theta)} = \frac{\partial w_h}{\partial r}\Big|_{(r=0,\theta)} = \frac{\partial w_h}{\partial r}\Big|_{(r=1,\theta)} = 0.$$

Starting with zero adhesion ($\ell = 0$) and gradually increase the load ℓ in fixed increments $\Delta\ell$, suppose that we have computed the solution $\Upsilon_\ell = \{\boldsymbol{\varphi}_\ell(\mathcal{A})\}$ using the b-spline reference surface $\Upsilon_\ell^0 = \{\boldsymbol{\varphi}_\ell^0(\mathcal{A})\}$. We expect that the solution $\Upsilon_{\ell+\Delta\ell}$ for loading $\ell + \Delta\ell$ to be close to Υ_ℓ. Although it is appealing to choose $\Upsilon_{\ell+\Delta\ell}^0 = \Upsilon_\ell$, this is not possible in general. First, Υ_ℓ is not a b-spline surface. In fact, $\boldsymbol{\varphi}_\ell : \mathcal{A} \to \mathbb{R}^3$ is not a piecewise polynomial (rather a piecewise rational polynomial). Second, the degree q and knot vectors T^0, S^0 used to define reference surfaces are chosen independently of degree p and knot vectors T, S used to approximate the offset coordinates. Hence we construct $\Upsilon_{\ell+\Delta\ell}^0$ to be an approximation of Υ_ℓ, by setting $\boldsymbol{\varphi}_{\ell+\Delta\ell}^0$ to be the $L^2(\mathcal{A})$-projection of $\boldsymbol{\varphi}_\ell$ onto $\mathbb{B}_{\mathrm{T}^0,q} \otimes \mathbb{B}_{\mathrm{S}^0,q}$. Specifically, $\Upsilon_{\ell+\Delta\ell}^0$ is defined by computing a new set of control points so that $\Upsilon_{\ell+\Delta\ell}^0$ approximates Υ_ℓ in an L^2-sense while satisfying boundary conditions (45). The example depicted in Fig. 1 was also computed in precisely this way.

We conclude this discussion with a few remarks.

(1) In Fig. 7, observe that the solutions at loads $\ell, \ell + \Delta\ell, \ldots$ are not graphical over the initial reference surface Υ_0^0, i.e., $\Upsilon_\ell, \Upsilon_{\ell+\Delta\ell} \ldots \not\subset \mathcal{N}(\Upsilon_0^0)$. Hence it is essential to update the choice of reference surfaces in this example (as well as in Fig. 1).

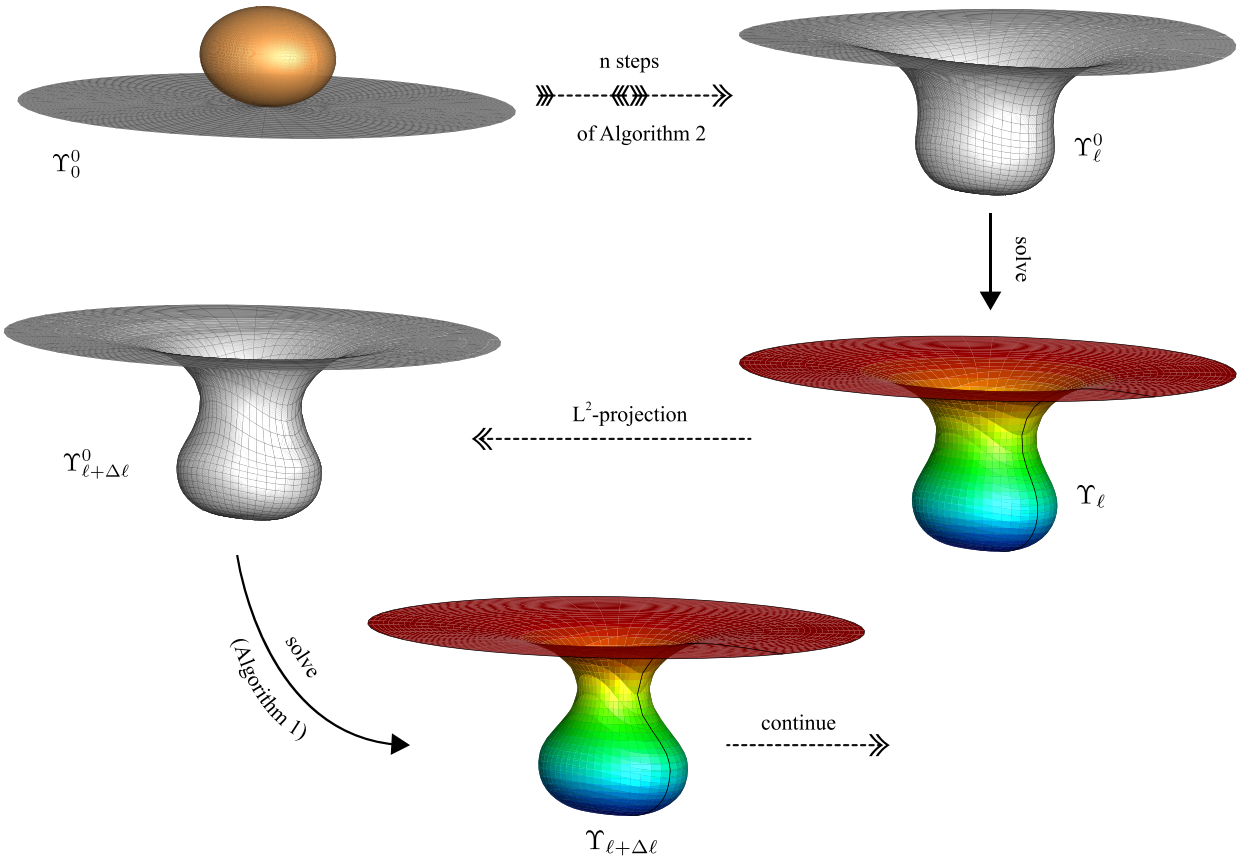

Fig. 7. Graphical illustration of Algorithm 2 using an example of a fluid membrane wrapping around an ellipsoidal particle. The load parameter ℓ corresponds to the adhesion energy γ in (56). To compute the solution $\Upsilon_{\ell+\Delta\ell}$ with load $\ell+\Delta\ell$, we construct the reference surface $\Upsilon_{\ell+\Delta\ell}^0$ as an approximation (L^2-projection) of the known solution Υ_ℓ at load ℓ.

(2) While Algorithm 2 updates the reference surface at each load step, it may only be necessary to perform such updates periodically.
(3) For definiteness, we retain the same knot vectors T^0 and S^0 for all reference surfaces in Algorithm 2. Such a choice, while convenient, is not essential. It is certainly possible, especially for solutions having localized features, to adapt the knot vectors used to define reference surfaces. In general, we may choose knot vectors T_ℓ^0, S_ℓ^0 and a corresponding set of control points $\{\mathbf{p}_{i,j}^0\}_{i,j}$ at load step ℓ to define the reference surface Υ_ℓ^0.
(4) Defining $\Upsilon_{\ell+\Delta\ell}^0$ to be an approximation of Υ_ℓ to solve problem $\mathbf{P}_{\ell+\Delta\ell}$ in Algorithm 2 should be interpreted in the context that $\Upsilon_{\ell+\Delta\ell}^0$ serves as an initial guess for the solution $\Upsilon_{\ell+\Delta\ell}$. The magnitude of the error in the computed solution w_h depends on the choice of the reference surface. However, we expect that small perturbations of the reference surface do not affect the order of accuracy of the solution. We do not present a rigorous analysis substantiating this intuition. The specific choice of an L^2-projection in Algorithm 2 is for convenience. Alternative methods of approximating Υ_ℓ to define $\Upsilon_{\ell+\Delta\ell}^0$ are certainly possible.
(5) The assumption that a small change in the loading parameter ℓ results in a small change in the solution Υ_ℓ (continuity) is essential for the success of Algorithm 2. It is possible to identify problems where this is not the case (the solution may suffer instabilities beyond certain ℓ, for example). Choosing the reference surface in such scenarios will presumably require detailed knowledge of the solution.

5. Specialization to axisymmetric configurations

We briefly discuss the specialization of the finite element method in Section 4 to axisymmetric membrane configurations. The assumption of rotational symmetry results in significant algorithmic and computational simplifications, besides being appropriate in a variety of experimentally-relevant applications. We provide examples in Section 5.2 and Section 5.3 to

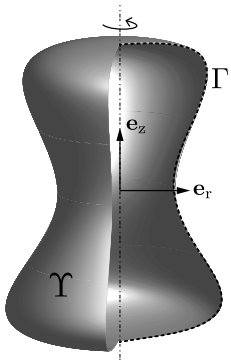

Fig. 8. An axisymmetric surface Υ defined by its generating curve Γ_g.

demonstrate using Algorithms 1 and 2 for the solution of the axisymmetric problem and discuss a few applications in Section 6 and Section 7.

5.1. The variational problem for offset axisymmetric fluid membranes

Axisymmetric surfaces are specified by their generating curve $t \mapsto (r(t), z(t))$ through parameterizations of the form

$$(\theta, t) \mapsto r(t)(\cos\theta\, \mathbf{e}_1 + \sin\theta\, \mathbf{e}_2) + z(t)\, \mathbf{e}_3 \quad \text{for } t \in \mathrm{I}, \theta \in 2\pi\mathrm{I}. \tag{46}$$

As depicted in Fig. 8, the surface in (46) possesses rotational symmetry about $\mathbf{e}_3$.

We seek axisymmetric solution surfaces of the form (46) for problem (**P**). To this end, we assume that both the reference surface Υ^0 and the offset coordinate w in (**P**) possess rotational symmetry. Let

$$\Gamma^0 := \{\boldsymbol{\psi}^0(t) \,:\, t \in \mathrm{I}, \boldsymbol{\psi}^0 \in \mathbf{V}_{\text{axi}} \cap (H^3[\mathrm{I}])^2\} \tag{47}$$

denote the generating curve for Υ^0, where the space $\mathbf{V}_{\text{axi}}$ incorporates appropriate boundary conditions on the parameterization $\boldsymbol{\psi}^0 = (r^0, z^0)$. The restriction of (**P**) to axisymmetric solution surfaces is the problem:

$$\boxed{\begin{aligned}&\text{Given } \Gamma^0 = \{\boldsymbol{\psi}^0(\mathrm{I})\}, \text{ find } (w, \lambda_A) \in H^2_0(\mathrm{I}) \times \mathbb{R} \text{ such that :}\\ &\qquad\qquad \langle \delta\Pi^{\text{axi}}[w, \lambda_A], (\delta w, \delta\lambda_A)\rangle = 0 \;\forall (\delta w, \delta\lambda_A) \in H^2_0(\mathrm{I}) \times \mathbb{R},\end{aligned}} \tag{$\mathbf{P}_{\text{axi}}$}$$

where

$$\Pi^{\text{axi}}[w] := \Pi^{\text{axi}}_B[w] + \lambda_A \Pi^{\text{axi}}_A[w] + \Pi^{\text{axi}}_F[w], \tag{48a}$$

$$\Pi^{\text{axi}}_B[w] := \frac{\kappa_b}{2} \int_I \mathrm{H}^2_{\text{axi}}\, \mathrm{J}_{\text{axi}}\, dt, \tag{48b}$$

$$\Pi^{\text{axi}}_A[w] := \int_I \mathrm{J}_{\text{axi}}\, dt, \tag{48c}$$

$$\Pi^{\text{axi}}_F[w] := \int_I \mu \mathrm{J}_{\text{axi}}\, dt. \tag{48d}$$

The generating curve of the solution Υ is given by

$$\Gamma := \{\boldsymbol{\psi}(t) = \boldsymbol{\psi}^0(t) + w(t)\mathbf{n}^0(t) : t \in \mathrm{I}\}, \tag{49}$$

where $\mathbf{n}^0$ denotes the unit normal to Γ^0. The functionals Π^{axi}, Π^{axi}_A, Π^{axi}_B and Π^{axi}_F in (48) are simply the restrictions of Π, Π_A, Π_B and Π_F to solution surfaces with rotational symmetry of the form (46) and with the generating curve (49). The coordinates (r, z) of $\boldsymbol{\psi}$ in the Cartesian basis $\{\mathbf{e}_r, \mathbf{e}_z\}$ and their derivatives with respect to parameter t appearing in (48) are computed as

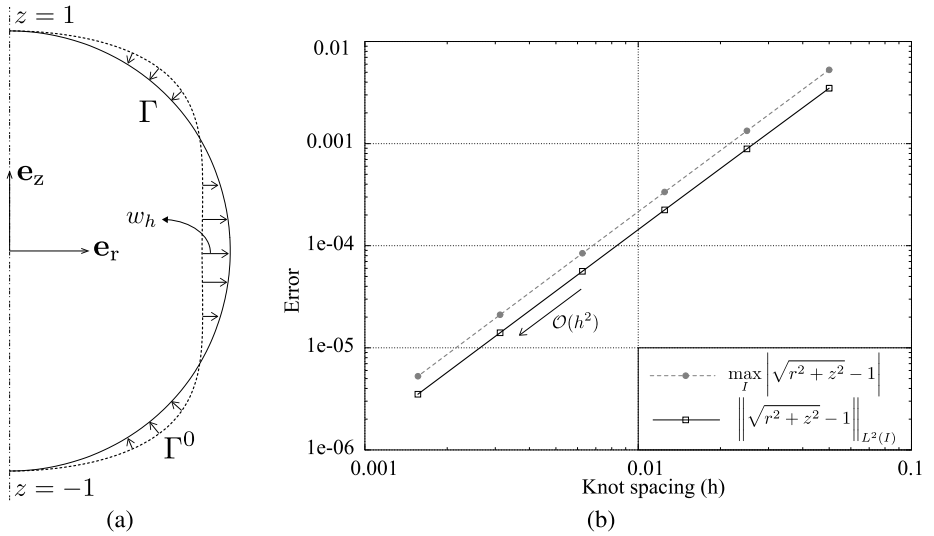

Fig. 9. Example illustrating the approximation of ($\mathbf{P}_{\text{axi}}$) using Algorithm 1. The reference curve Γ^0 shown in dotted lines on the left is a cubic b-spline curve satisfying boundary conditions (52). The equilibrium configuration is computed by interpolating w_h quadratic b-spline shape functions. The plot on the right shows the convergence of solutions as the knot spacing is reduced, while using the same reference curve Γ^0.

$$
\begin{aligned}
r &= r_0 + w\,(\mathbf{n}_0 \cdot \mathbf{e}_r)\\
r' &= r_0' + (w'\mathbf{n}_0 + w\mathbf{n}_0') \cdot \mathbf{e}_r\\
r'' &= r_0'' + (w''\mathbf{n}_0 + 2w'\mathbf{n}_0' + w\mathbf{n}_0'') \cdot \mathbf{e}_r\\
z &= z_0 + w\,(\mathbf{n}_0 \cdot \mathbf{e}_z)\\
z' &= z_0' + (w'\mathbf{n}_0 + w\mathbf{n}_0') \cdot \mathbf{e}_z\\
z'' &= z_0'' + (w''\mathbf{n}_0 + 2w'\mathbf{n}_0' + w\mathbf{n}_0'') \cdot \mathbf{e}_z\\
\alpha &= r'z'' - r''z'\\
\beta &= \sqrt{r'^2 + z'^2}\\
\mathrm{J}_{\text{axi}} &= 2\pi r\beta\\
\mathrm{H}_{\text{axi}} &= \frac{1}{\beta}\left(\frac{\alpha}{\beta^2} + \frac{z'}{r}\right).
\end{aligned}
\tag{50}
$$

Analogous to (**G**), the Galerkin approximation of problem (47) is obtained by restricting the offset field w in (47) to a finite dimensional subspace $V_{1\mathrm{D}}$ of $H_0^2(\mathrm{I})$,

$$
\begin{aligned}
&\text{Given } \Gamma^0 = \{\boldsymbol{\psi}^0(\mathrm{I})\}, \text{ find } (w_h, \lambda_h) \in V_{1\mathrm{D}} \times \mathbb{R} \text{ such that :}\\
&\qquad \langle \delta\Pi^{\text{axi}}[w_h, \lambda_h], (\delta w_h, \delta\lambda_h)\rangle = 0 \;\forall (\delta w_h, \delta\lambda_h) \in V_{1\mathrm{D}}^{\partial} \times \mathbb{R},
\end{aligned}
\tag{$\mathbf{G}_{\text{axi}}$}
$$

where $V_{1\mathrm{D}}^{\partial}$ is the space of admissible variations of $V_{1\mathrm{D}}$. In the remainder of the article, we shall adopt $V_{1\mathrm{D}} = \mathbb{B}_{\mathrm{T},p}$. The components of the finite element residual vectors and tangent matrices can be derived using the calculations in Section 3.4 in conjunction with (46) and (49). We provide detailed expressions for them in Appendix A. Finally, analogous to our construction of reference surfaces as b-spline surfaces in Section 4.3 and Section 4.4, we construct reference generating curves as b-spline curves. Hence the parameterization $\boldsymbol{\psi}^0$ of Γ^0 in (47) is of the form

$$
\boldsymbol{\psi}^0(t) := \sum_{a=0}^{n'+q-1} \mathbf{p}_a^0 N_{a,q}(t),\ t \in \mathrm{I},
\tag{51}
$$

where $\{\mathbf{p}_a^0\}_a$ are the control points of Γ^0.

5.2. Example: optimal convergence using Algorithm 1

Fig. 9 shows an example computed using Algorithm 1 to approximate the solution of ($\mathbf{P}_{\text{axi}}$). We assume that there are no external interactions ($\Pi_F = 0$), omit the area constraint ($\lambda_A = 0$), and impose boundary conditions

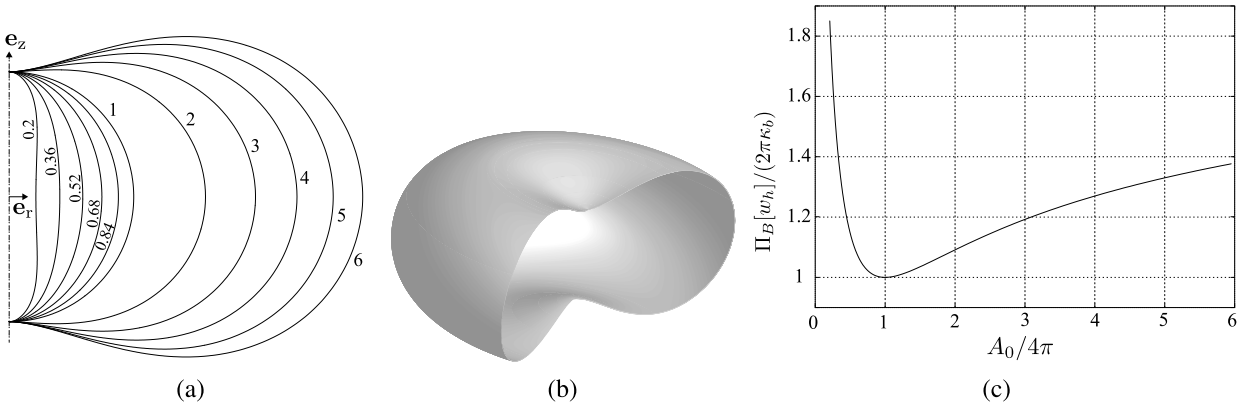

Fig. 10. Calculation of equilibrium vesicles shapes as the prescribed surface area is varied incrementally. Solutions computed using Algorithm 2 are depicted on the left. The solution computed with prescribed surface area A_0 is used to construct the reference curve for computing the solution with surface area $A_0 + \Delta A_0$, where ΔA_0 is a small increment. Figure (b) shows the biconcave shape realized for a specific value of the prescribed surface area, which corresponds to a reduced volume $v := 6\sqrt{\pi}V_0/(A_0)^{3/2} = 0.8$. The bending energy of the vesicle is plotted on the right as a function of its surface area. The minimum occurs, as expected, for the case of a unit sphere.

$$\begin{cases} r(0) = r(1) = 0, \\ z(0) = 1, \\ z(1) = -1, \\ z'(0) = z'(1) = 0, \end{cases} \tag{52}$$

for coordinates (r, z) of the solution Γ. The exact solution of ($\mathbf{P}_{\text{axi}}$) is hence the unit circle centered at $(1/2, 0)$.

In Fig. 9(a), the reference curve Γ^0 is a cubic b-spline, with its 13 control points chosen such that the coordinates (r^0, z^0) of Γ^0 satisfy boundary conditions (52). The offset coordinate is approximated using 22 quadratic b-spline functions ($p = 2$), a knot vector with uniform spacing $h = 1/20$ and satisfies boundary conditions $w_h(0) = w_h(1) = w_h'(0) = w_h'(1) = 0$.

Fig. 9(b) examines the convergence of computed generating curves to the exact one, as the knot spacing h is reduced while maintaining $p = 2$ and Γ^0 fixed. We see that the rate of convergence in the $L^2(\mathrm{I})$-norm is optimal, as was the case in the example in Section 4.2. The error in the max-norm is also observed to converge as $\mathcal{O}(h^2)$. We mention that for a given Γ^0 and knot vector, the accuracy of the solution can be improved by increasing the degree of b-splines used to interpolate w_h.

5.3. Example: incremental solutions using Algorithm 2

Fig. 10 shows an example using Algorithm 2 to compute axisymmetric solutions in a sequence of incrementally loaded problems, with the prescribed surface area of the fluid membrane serving as the loading parameter. Hence the solution computed with surface area A_0 serves to construct the reference curve used to compute the solution with surface area $A_0 + \Delta A_0$.

In the example in Fig. 10, each reference curve is a cubic b-spline with 23 control points and satisfies boundary conditions (52). At each loading step, normal perturbations w_h satisfy boundary conditions $w_h(0) = w_h'(0) = w_h(1) = w_h'(1) = 0$, and are interpolated using 52 quadratic b-spline functions defined on a uniformly spaced knot vector. Control points for the reference curve are recomputed (using an $L^2(\mathrm{I})$-projection) at the end of each load step. The figure also shows the realization of a biconcave shape with increasing surface area, a characteristic of red blood cells.

6. Application: adhesive interaction with rigid substrates

We demonstrate a useful application of the proposed finite element method to studying adhesive interactions of axisymmetric fluid membranes with rigid substrates. We consider two simple adhesion models. The first one discussed in Section 6.1 has been previously considered in [48,49], while the second type of interaction described in Section 6.3 is inspired by cohesive zone models in fracture mechanics [50]. The two models are qualitatively similar. Both consider adhesion to be a finite range interaction and are each defined by two parameters— the adhesion energy at the surface of the substrate and a length scale dictating the range of adhesive interactions. As this length scale approaches zero, we recover, at least in a qualitative sense, a contact-type potential.

The rationale behind adopting potentials that explicitly introduce a length scale for the interaction, rather than assuming a contact potential, is two fold. First, experiments show that there is indeed a finite separation between interacting membranes. We interpret such a separation as the cumulative effect of various interactions, for instance van der Waals forces, electrostatic repulsion, steric interactions, and the formation of bonds between complimentary surface ligands and receptors [51]. The second reason arises from the need for tracking the adhesion front when using a contact potential. Specifically,

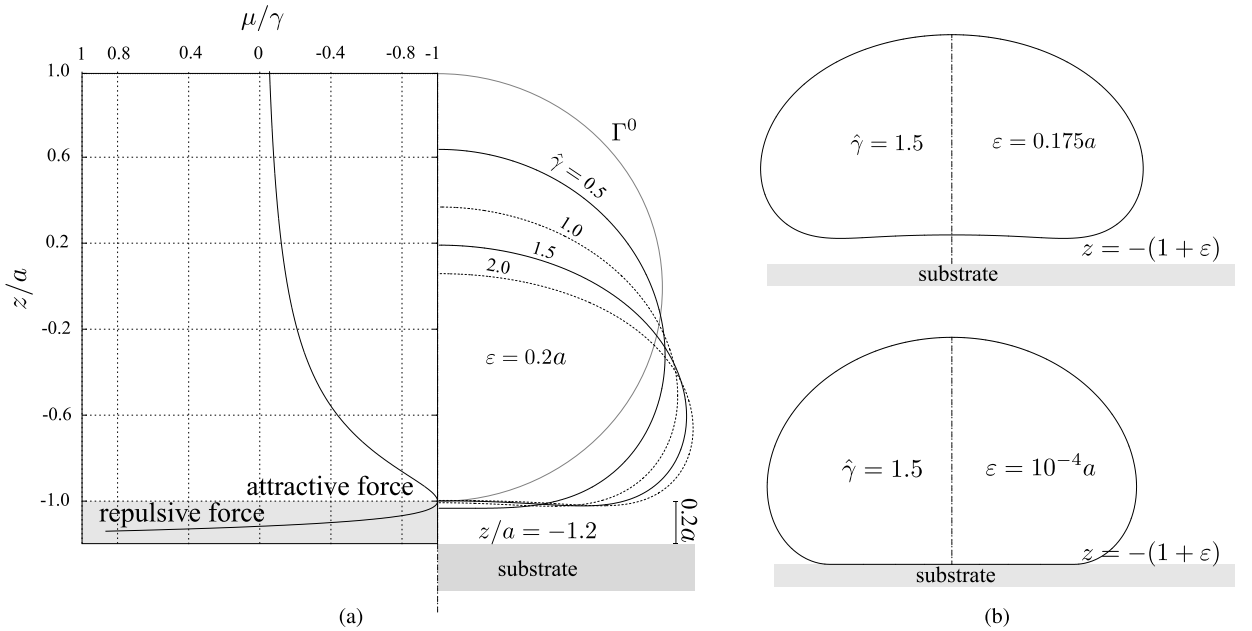

Fig. 11. Deformation of a vesicle due to the adhesive potential (53). Figures (a) and (b) illustrate the influence of the non-dimensionalized adhesion energy $\hat{\gamma}$ and the length-scale ε, respectively.

a contact potential introduces a moving interface that distinguishes the region of the membrane adhered to the substrate from that which is not. Analogous to a displacement discontinuity in a fractured solid, the membrane suffers a sharp jump in curvature across the adhesion front. For axisymmetric problems, this is not a particularly difficult issue since tracking the adhesion front reduces to following a corresponding point on the curve generating the membrane surface. For general three-dimensional membranes however, tracking a moving front introduces additional complexities that include describing the interface, defining compatible discretizations on either side of it and accounting for changes in topology of the interface.

6.1. Adhesion of vesicles in a finite range potential

Consider a flat substrate occupying the region $z \le z_s$. Let the interaction of a lipid molecule with the substrate be governed by the potential

$$\mu(z) = \gamma \left[\left(\frac{\varepsilon}{z - z_s} \right)^2 - 2 \left(\frac{\varepsilon}{z - z_s} \right)^4 \right], \tag{53}$$

which depends on the distance $z - z_s$ normal to the substrate and attains a minimum value of $-\gamma$ at $z - z_s = \varepsilon$, see Fig. 11(a). The parameter γ is interpreted as the adhesion energy per unit area while the length scale ε defines the range of interaction away from the substrate. Within the framework of the model problem ($\mathbf{P}_{\text{axi}}$), we set Π_F to be

$$\Pi_F[w] = \int_0^1 \mu(z(w))\, 2\pi r \beta \, dt. \tag{54}$$

In addition to (54), we assume boundary conditions

$$\begin{cases} r(0) = r(1) = 0, \\ z'(0) = z'(1) = 0, \end{cases} \tag{55}$$

for the coordinates (r, z) of the solution and impose the surface area constraint

$$\Pi_A = \int_I 2\pi r \beta \, dt = 4\pi a^2, \text{ where } a = 1.$$

We choose the reference curve Γ^0 to be a semi-circle with radius $a = 1$ that satisfies boundary conditions (55). Boundary conditions on the offset coordinate then follow as $w_h'(0) = w_h'(1) = 0$. Notice that the axial coordinates at the poles are unconstrained, i.e., $z(0)$ and $z(1)$ are not prescribed. They are determined by the values of $w_h(0)$ and $w_h(1)$, which are in turn computed as part of the solution.

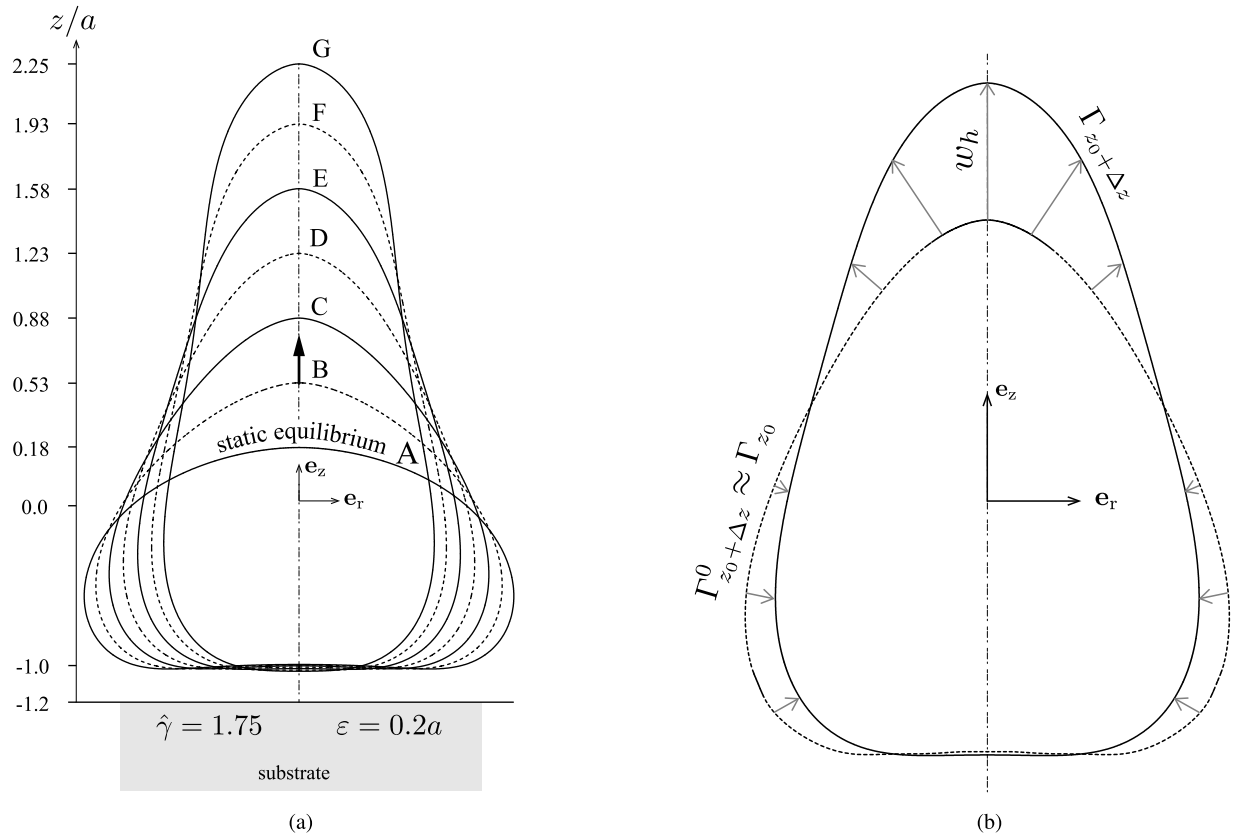

Fig. 12. Manipulation of a vesicle adhered to a substrate simulated using Algorithm 2. In figure (a), a prescribed displacement is imposed at the top of an adhered but otherwise unconstrained vesicle. The vesicle remains adhered to the substrate even after a displacement of over twice its radius. Figure (b) shows the reference curve used to compute one of the intermediate configurations.

Fig. 11(a) examines the deformation of a vesicle as the non-dimensional parameter $\hat{\gamma} := \gamma/(\kappa_b a^2)$ is varied, while Fig. 11(b) demonstrates the influence of the length scale ε. The vesicle shapes are computed following Algorithm 1 and using 200 cubic b-splines for interpolating w_h. When $\hat{\gamma} = 0$, the exact solution coincides with Γ^0 irrespective of the choice of ε. At finite values of $\hat{\gamma}$, observe from the figure that the vesicle appears tethered at $z \approx z_s + \varepsilon$, i.e., at a distance ε away from the surface of the substrate. For a fixed ε, we see that the contact area and the deformation of the vesicle increase with $\hat{\gamma}$. Decreasing ε, and in particular the case $\varepsilon = 10^{-4}a$ in Fig. 11(b), reveals that the interaction (53) progressively resembles a contact-type potential.

The choice of a semi-circle as a reference curve in Fig. 11 is appropriate because the range of deformations examined is sufficiently small. When the top pole of the vesicle approaches the center of Γ^0 at larger values of $\hat{\gamma}$, it is necessary to adopt a new reference curve and follow Algorithm 2.

6.2. Manipulation of an adhered vesicle

The peel test is a commonly used experimental technique to quantify the strength of adhesion between a vesicle and a substrate. It consists in measuring the force/energy required to detach an adhered vesicle from the substrate. Such measurements can also help calibrate parameters in a model such as (53). Here we simulate a displacement-controlled test in which a prescribed displacement is imposed at the top pole of the vesicle away from the substrate. The problem setup is identical to that in Section 6.1, except that $z(1) = z_{\text{top}}$ is prescribed. Hence we set $z^0(1) = z_{\text{top}}$ and $w_h(1) = 0$.

Fig. 12(a) shows the equilibrium configurations of the vesicle corresponding to parameters $\hat{\gamma} = 1.75$ and $\varepsilon = 0.2a$, as the top pole is displaced away from the substrate. The solutions were computed using Algorithm 2, with the imposed displacement serving as the loading parameter. Rather than updating the reference curve with each displacement increment, it was updated periodically; Fig. 12(b) shows the reference curve used to compute one of the intermediate shapes.

Accurate detection of the detachment of the vesicle from the substrate requires identifying a bifurcation in the load-displacement curve. We adopt an alternative strategy shown in Fig. 13. To identify the transition between adhered and detached states, we consider the total energy when (i) the attached vesicle is pulled away from the substrate and (ii) as a detached vesicle is brought towards the substrate from sufficiently far away. The prescribed position z_{top} at which these two energy curves meet identifies two distinct equilibrium configurations of the vesicle, corresponding to an adhered and

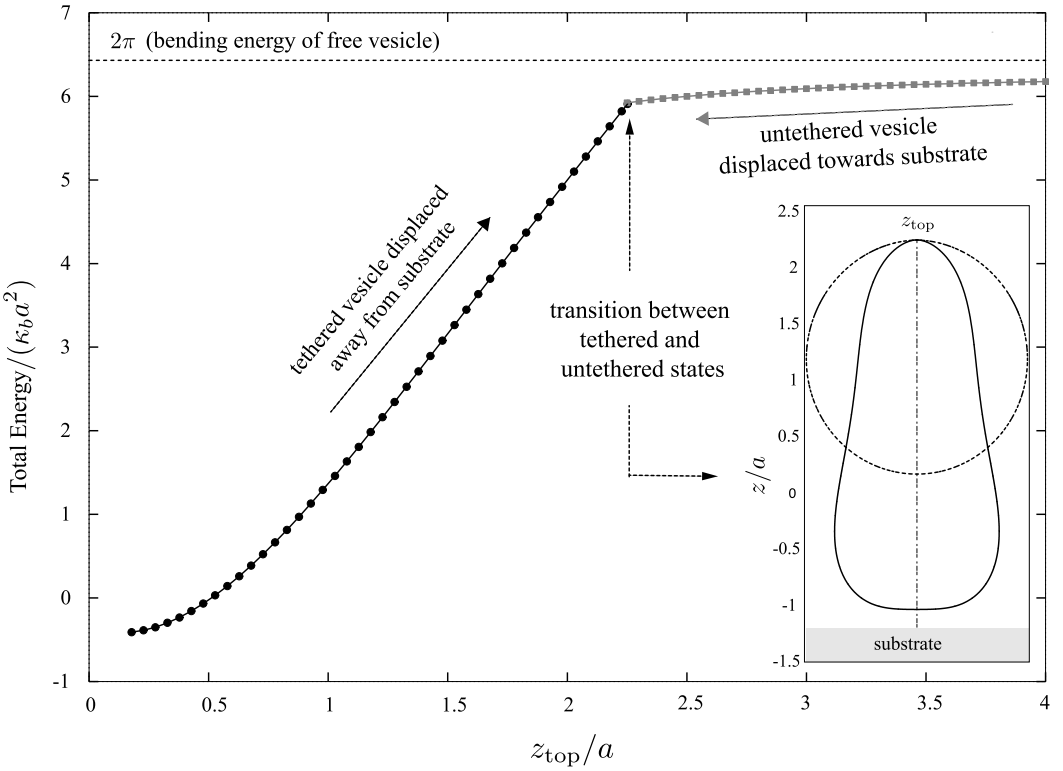

Fig. 13. Detachment of a vesicle adhered to a substrate in a displacement-controlled test. The plot shows the total energy of a vesicle in two tests— as an adhered vesicle is pulled away from the substrate and as a detached vesicle is brought progressively closer to the substrate from far away. The prescribed position of the top of the vesicle at which the two energy curves meet identifies the transition between adhered and detached states.

a detached state, that have identical energy. For the chosen values of $\hat{\gamma}$ and ε, we find this position to be $z_{\text{top}} \approx 2.25a$. Fig. 13 shows the two configurations computed at this point. The figure also indicates the energies corresponding to the configurations shown in Fig. 12(a). In the regime $z_{\text{top}} > 2.25a$, the vesicle has lower energy in a detached state while the adhered state is only metastable. Conversely, for $z_{\text{top}} < 2.25a$, the detached state is metastable while the adhered state has a lower energy.

6.3. Uptake of a spherical particle by a fluid membrane

Next, we study the uptake of a rigid spherical particle by a fluid membrane [52–54]. We consider the setup depicted in Fig. 14(a) in which a circular fluid membrane with radius $a = 1$ is connected to a lipid reservoir along its periphery. A rigid spherical particle, coated with ligands capable of binding with receptors on the membrane, is introduced at the center of the membrane. The energy released by the formation of ligand-receptor bonds induces deformation of the membrane, causing the membrane to wrap around the particle. The excess lipids (surface area) necessary for this wrapping are supplied by the reservoir. The kinetics of membrane receptors is an important factor in the dynamic wrapping process [34,55]. Here we assume the receptor supply to be indefinite and instantaneous, so that we may consider the problem to be quasistatic. We are exclusively concerned with determining the deformation of the fluid membrane around the particle as a function of the adhesion energy, which is roughly correlated to the density of ligands on the particle.

We consider an adhesive potential $\Phi : \mathbb{R} \to \mathbb{R}$ that is qualitatively similar to (53) and given by

$$\Phi(\phi_p) := -\gamma \left(1 + \frac{\phi_p}{\varepsilon}\right) \exp\left(-\frac{\phi_p}{\varepsilon}\right). \tag{56}$$

The argument ϕ_p of Φ is the signed distance to the particle surface Γ_p

$$\phi_p(r, z) := \sqrt{r^2 + (z - r_p)^2} - r_p,$$

where r_p is the radius of the particle centered at $(0, r_p)$ and we adopt the convention of negative distances within the particle. Notice that Φ attains a minimum value of $-\gamma$ at Γ_p where $\phi_p = 0$. As in (53), the parameter γ is the adhesion energy per unit area. The length scale ε determines the rate of decay of the interaction away from Γ_p, as well as the rate of growth within the particle. The latter behavior serves to enforce a penalty for penetration of the membrane into the particle. These features of (56) are illustrated in Fig. 14(b).

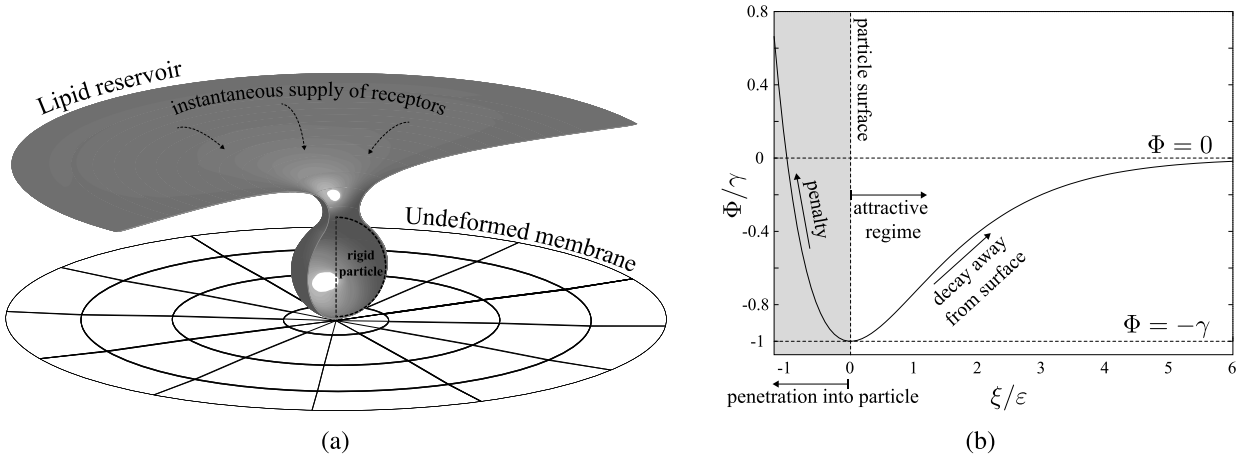

Fig. 14. An initially flat membrane spontaneously wraps around a rigid particle, either completely or partially when the energy released due to adhesion compares favorably with the energetic cost of membrane deformation. We assume that the excess membrane area required for wrapping is supplied by a lipid reservoir along the membrane boundary and neglect the kinetics of receptor diffusion responsible for adhesion of the membrane to the particle. The deformed membrane shape shown in (a) corresponds to the configuration depicted in Fig. 15(d). The features of the potential (56) used to model adhesion are illustrated in (b).

In the context of problem ($\mathbf{P}_{\text{axi}}$), Π_F has the form

$$\Pi_F[w] := \int_0^1 \Phi(\phi_p(r,z))\, 2\pi r \beta \, dt. \tag{57}$$

The explicit appearance of the signed distance to the particle surface in (56) and (57) conveys the influence of the geometry of the particle on the deformation of the membrane. The influence of the particle geometry on the weak form is evident from the linearization of Π_F,

$$\langle \delta\Phi(\phi_p(r,z)), \delta w \rangle = \Phi'(\phi_p(r,z))\, \mathbf{n}_p(\pi_p(r,z)) \cdot \mathbf{n}^0, \tag{58}$$

where $\mathbf{n}_p$ is the unit outward normal to Γ_p and π_p is the closest point projection onto Γ_p. Similarly, computing the second variation of Π_F introduces the influence of the curvature of Γ_p.

For simplicity, we assume that the particle remains fixed and allow the membrane to deform around it. Correspondingly, we assume boundary conditions

$$\begin{cases} r^0(0) = 0 \\ r^0(1) = a \\ z^{0\prime}(0) = z^{0\prime}(1) = 0 \\ w_h'(0) = w_h'(1) = 0, \end{cases} \tag{59}$$

for the coordinates (r^0, z^0) of the reference curve and the offset coordinate w_h. Fig. 15 depicts the results from a calculation following Algorithm 2, using cubic b-splines to interpolate w_h, with the radius of the particle set to $r_p = 0.15a$, length scale $\varepsilon = 10^{-2}a$, and as the non-dimensional parameter $\hat{\gamma} = \gamma/(\kappa_b a^2)$ is increased in steps of $\Delta\hat{\gamma} = 0.5$.

The deformation of the membrane around the particle results from a competition between the energy gained from adhesion and the cost of membrane deformation. Fig. 16(a) shows the bending energy and the contact area as a function of $\hat{\gamma}$. The contact area is computed as the ratio $\Pi_F[w_h]/\gamma$. As $\hat{\gamma}$ is increased, we observe that the contact area approaches that of the surface area of the particle, indicating complete wrapping. Fig. 16(b) shows the distribution of the mean curvature as a function of the parametric coordinate $t \in \mathrm{I}$ for the case $\hat{\gamma} = 32$. We observe that the curvature is close to that of the particle $(1/r_p)$ where the membrane is adhered to the particle, undergoes a sharp drop and subsequently reaches zero. With a contact potential, the membrane curvature suffers a discontinuity at the interface between adhered and detached regions of the membrane. Since we adopt a regularized potential (56), we observe a sharp but continuous change in curvature instead. The total surface area of the membrane increases by about 10% in the configuration in Fig. 15(d). Since we have assumed zero membrane tension, there is no energy associated with drawing additional lipids from the reservoir.

7. Application: tether formation

Biological membranes exhibit numerous tubular structures along their periphery. Such tether-like structures are thought to form as a result of localized forces exerted by external proteins. Besides their biological significance, experiments to

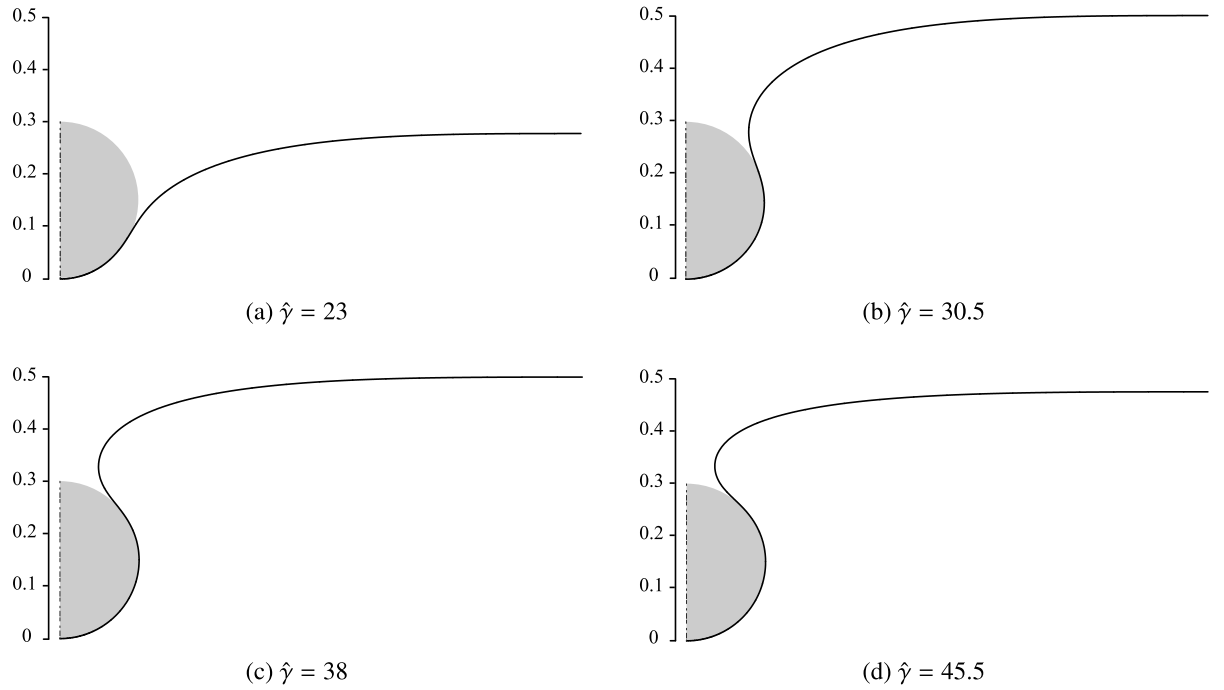

Fig. 15. Wrapping of a fluid membrane with unit radius around a spherical particle with radius $r_p = 0.15a$ as a function of increasing adhesion energy. Adhesion between the membrane and the particle is modeled with the potential in (56). Membrane deformations are computed using Algorithm 2.

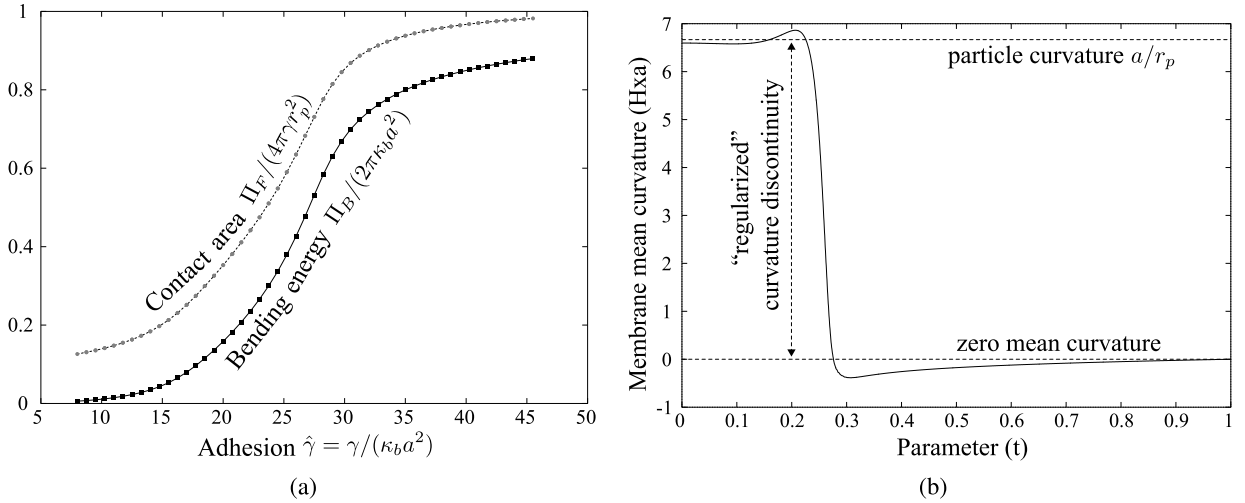

Fig. 16. Plot (a) shows the bending energy and contact area as a function of the adhesion energy $\hat{\gamma}$ for the example discussed in Section 6.3. With increasing $\hat{\gamma}$, the contact area approaches that of the surface area of the particle indicating complete wrapping. The bending energy approaches that of a spherical vesicle. The markers in the plot indicate calculations using quartic b-splines for the offset coordinate and quintic b-splines for the reference curve. The solid and dashed lines correspond to using cubic and quartic b-splines, respectively. The agreement between the two calculations suggests that the results have converged. Plot (b) shows the mean curvature as a function of the curve parameter t for $\hat{\gamma} = 32$. Notice the sharp drop at the transition from adhered to the detached region of the membrane.

measure mechanical properties of membranes routinely use optical tweezers or micropipettes to pull tethers from membranes [41,56].

7.1. Tether formation in flat membranes

Roughly speaking, a membrane subjected to a point force/displacement prefers a diffuse (non-local) deformation that minimizes its bending energy. Membrane tension on the other hand serves to localize the deformation in order to reduce the energetic cost associated with a larger surface area. Fig. 17 shows an example computed using Algorithm 2 to illustrate the role of membrane tension in the formation of tethers [57,58]. We consider an initially flat membrane (representative of

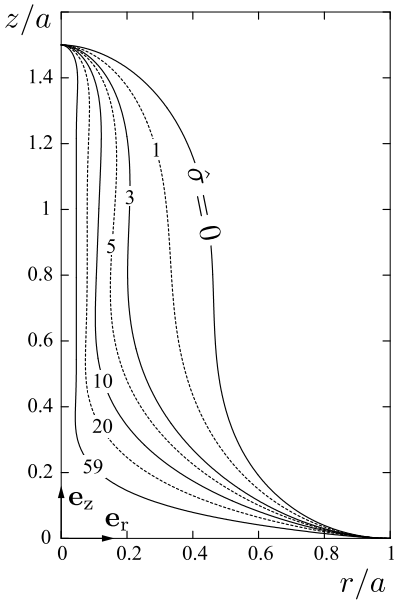

(a) Tether shapes for $L = 1.5a$, and various $\hat{\sigma}$

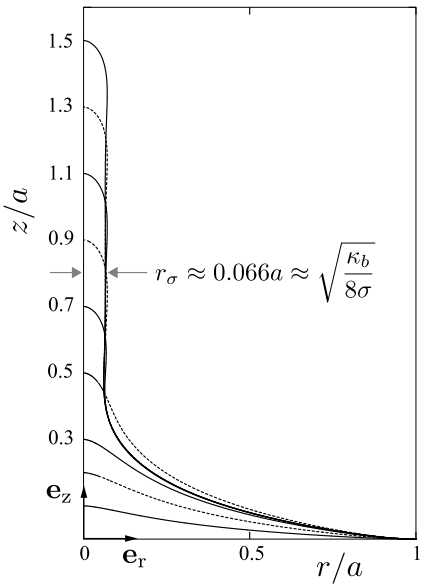

(b) r_σ as a function of L for $\hat{\sigma} = 29$

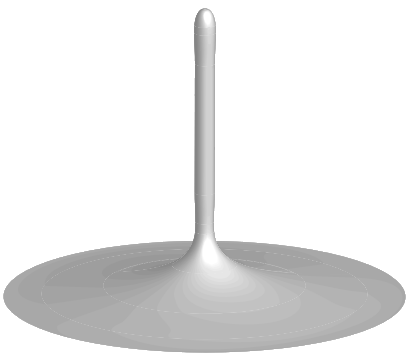

(c) Tether shape at $L = 1.5a, \hat{\sigma} = 59$

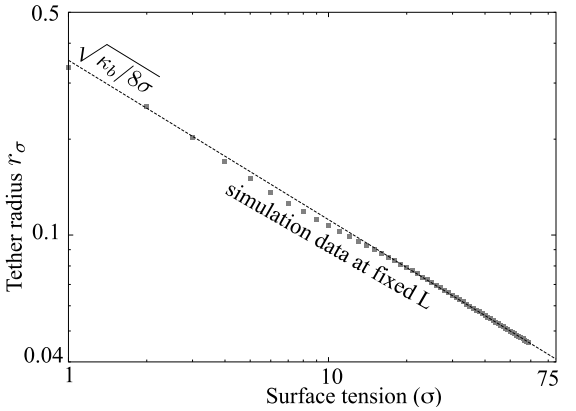

(d) Numerical evidence supporting the relation $r_\sigma \sim (\kappa_b/\sigma)^{1/2}$

Fig. 17. Demonstration of tether formation in membranes with membrane tension. Figure (a) shows the localization of membrane deformation with increasing tension. Figure (b) shows that at fixed $\hat{\sigma} \gg 1$, the tether radius r_σ is independent of the tether length L. Plot (d) demonstrates that r_σ scales as $(\kappa_b/\sigma)^{1/2}$ when $\hat{\sigma} \gg 1$, as predicted by (61).

a giant vesicle) with radius $a = 1$. The membrane is clamped along its periphery to a lipid reservoir. A prescribed displacement is imposed at its center to replicate a displacement-controlled experimental. Correspondingly, we assume boundary conditions

$$\begin{cases} r^0(0) = 0 \\ r^0(1) = a \\ z^0(0) = L \\ z^0(1) = 0 \\ z^{0\prime}(0) = z^{0\prime}(1) = 0 \\ w_h(0) = w_h(1) = w_h'(0) = w_h'(1) = 0, \end{cases}$$

for the reference curve and offset coordinate. A given tension σ in the membrane contributes to the energy functional Π in $(\mathbf{P}_{\text{axi}})$ as

$$\Pi_F[w] := \sigma \int_0^1 2\pi r \beta \, dt.$$

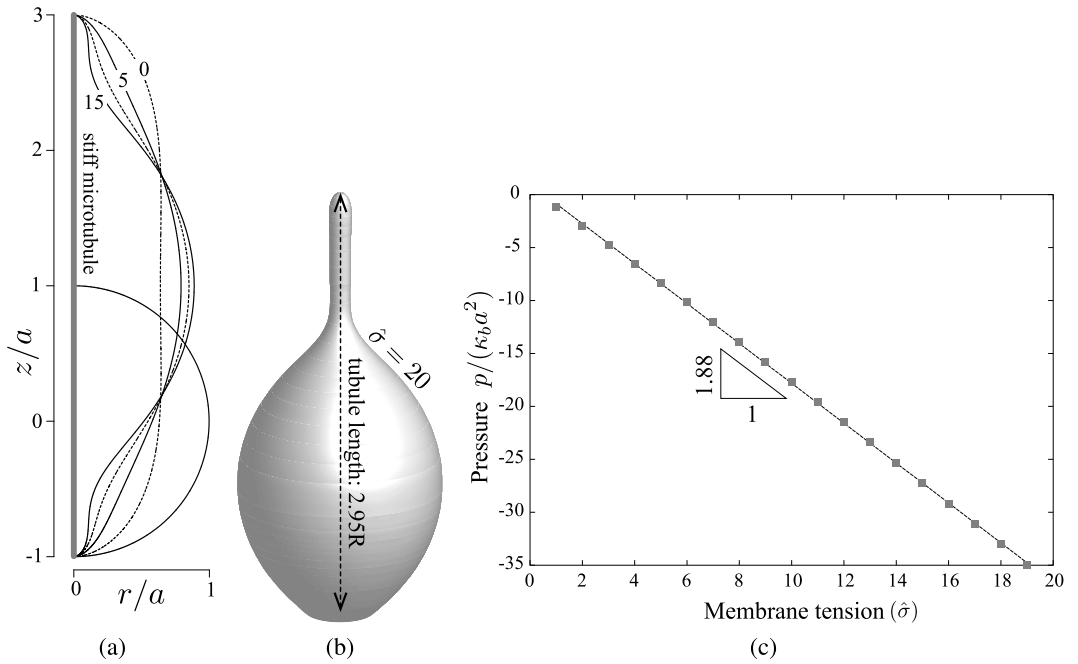

Fig. 18. Deformation of a vesicle containing a rigid tubule with increasing membrane tension. Figure (a) depicts the vesicle shapes realized (computed) for a fixed tubule length $L \sim 3a$ as $\hat{\sigma}$ is increased. Both symmetric and asymmetric vesicle shapes are possible, as evidenced by figures (a) and (b). Figure (c) shows the pressure in the (incompressible) fluid contained in the vesicle as a function of $\hat{\sigma}$ for a given tubule length $L \sim 3a$. The linear relationship observed suggests that when the surface energy from membrane tension dominates the bending energy of the vesicle, a simple Laplace–Young relation provides a reasonable estimate for the fluid pressure.

At a fixed displacement L at the center of the membrane, Fig. 17(a) depicts the shapes realized for a few different values of the non-dimensional parameter $\hat{\sigma} := \sigma/(\kappa_b a^2)$. We see that the membrane deformation is progressively localized to a small vicinity of the center with increasing values of $\hat{\sigma}$. When $\hat{\sigma} \gg 1$, a simple calculation helps estimate the radius r_σ of the tether. Assuming that the cylindrical tether structure contributes exclusively to the bending and surface energies, we have

$$\Pi \approx \frac{\kappa_b}{2} \times \frac{1}{4r_\sigma^2} \times 2\pi r_\sigma L + \sigma \times 2\pi r_\sigma L + \text{external work}, \tag{60}$$

in which the first term is the bending energy and the second is the contribution from membrane tension. The third term in (60) represents the work done in extending the tether to its length L. Requesting stationarity of Π in (60) with respect to r_σ and noting that the external work is independent of r_σ, we get

$$\sigma \gg \kappa_b/a^2 \;\Rightarrow\; r_\sigma \approx \sqrt{\frac{\kappa_b}{8\sigma}}. \tag{61}$$

The estimate for r_σ in (61) is independent of the tether length L, the membrane radius a and scales as $\sigma^{-1/2}$. These features are evident in the numerically computed solutions as well. Fig. 17(b) shows the membrane deformation for $\hat{\sigma} = 29$ as the tether length L is varied. The measured tether radius agrees well with (61) and notably, found to be independent of L. Fig. 17(d) compares the estimate in (61) with the radii measured from membrane deformations computed for a range of $\hat{\sigma}$ while using a fixed length $L = 1.6a$. We observe good agreement between the two when $\hat{\sigma} \gg 1$.

7.2. Microtubules in vesicles

Actin polymerization in migrating cells causes the formation of slender extensions of the membrane for purposes of sensing the environment during cell migration [59]. Such behavior can be modeled, in a very simplified setting, using membrane tension in finite-sized vesicles. Membrane tension also dominates the behavior of vesicles in biomechanical force probes used to characterize the mechanical response of single bonds [56].

In Fig. 18, we consider an application relevant to measuring the bending rigidity of microtubules [60]. In such measurements, a microtubule (or a bundle of them) is contained within a vesicle. The length of the tubule is larger than the diameter of the vesicle, causing the vesicle to deform. The membrane tension in the vesicle is controlled using micropipette aspiration, without altering the volume of the fluid in the vesicle. Since the bending stiffness of tubules is much larger that of the vesicle, we assume the tubules to be rigid. We also neglect possible adhesion of the membrane to the tubule

wall, which is reasonable when the diameter of tubules is 2–3 orders of magnitude smaller than its length and the vesicle diameter. The measurement of the bending modulus of the tubule itself relies on the buckling of the tubule triggered by a sufficiently large membrane tension; we do not simulate this phenomenon here.

For a vesicle of radius $a = 1$, Fig. 18(a) shows the vesicle shapes realized for a given tubule length L as the parameter $\hat{\sigma} := \sigma/(\kappa_b a^2)$ is increased. The volume enclosed by the vesicle is maintained at $V_0 = (4/3)\pi a^3$. We assume boundary conditions

$$\begin{cases} r^0(0) = r^0(1) = 0 \\ z^0(0) = z^{0'}(0) = z^{0'}(1) = 0 \\ z^0(1) = L \\ w_h(0) = w_h'(0) = w_h(1) = w_h'(1) = 0, \end{cases}$$

for the reference curve and offset coordinate. We observe that increasing the membrane tension causes the deformation of the vesicle to localize around the microtubules. In contrast to the symmetric shapes seen in Fig. 18(a), Fig. 18(b) shows a vesicle configuration that is asymmetric in the vertical direction. It is identified by perturbing the initial guess used to compute the symmetric solution. Both symmetric and asymmetric shapes have been previously reported [61]. Their energies were almost identical in our calculations.

From the vesicle shapes observed in Fig. 18(a), it is evident that the approximations employed in computing the tether radius for a flat membrane in (61) are no longer warranted. Nevertheless, we see from Fig. 18(b) that the pressure p, computed as the Lagrange multiplier conjugate to the volume constraint, exhibits a simple linear relationship with the membrane tension for a fixed tubule length. The data shown in Fig. 18(b) demonstrates that the Young–Laplace relation $p \approx -2\sigma a$ provides a reasonable approximation for the pressure in the fluid enclosed by the vesicle.

8. Concluding remarks

We introduced a simple and efficient finite element method to systematically approximate large deformations of three-dimensional fluid membranes at equilibrium. The method is devoid of artificial constraints and stabilizations for in-plane fluid motion, as is commonly found in the literature on this topic. The choice of (the normal offset) coordinate addresses an important oversight in the literature wherein numerical computations have predominantly been restricted to Cartesian coordinates. Yet, the proposed method does not explicitly require computing detailed differential-geometric quantities and is reasonably straightforward to implement.

We anticipate applications of the proposed method to a wider class of experimentally relevant problems (tweezers, micropipette aspirations, vesicle packaging of nano-materials) as well as problems with important additional physics. In the latter category, we are particularly interested in studying optimal shapes, sizes and orientations of nano-particles in endocytosis while including the diffusion of membrane receptors [62–65], in investigating mechanisms of phagocytosis [66] and understanding vesicle interactions with encapsulated filaments [60]. Recent advances in defining smooth discretizations over adaptively refined grids will be crucial for efficiently computing general three-dimensional solutions in such applications.

Appendix A. Operator expressions for the axisymmetric case

The expressions for the weak form and its linearization recorded in Section 3.4 simplify significantly for axisymmetric membrane configurations. We provide the expressions for the residual $\mathbf{R}^{\text{axi}}[w_h, \lambda_h]$ and the tangent $\mathbf{A}^{\text{axi}}[w_h, \lambda_h]$ operators, while assuming that the offset coordinate w_h is interpolated in the space of b-spline functions of degree p, i.e., $V_{1\text{D}} = \mathbb{B}_{\text{T},p}$.

A.1. Evaluation of the residual (weak form)

The residual $\mathbf{R}^{\text{axi}}[w_h, \lambda_h]$ is evaluated by linearizing the functional Π^{axi} in (48) along admissible variations. Adopting the shorthand $\delta_a(\cdot) = \langle \delta(\cdot), N_{a,p} \rangle$, we have

$$\mathbf{R}_a^{\text{axi}}[w_h, \lambda_h] := \mathbf{F}_a^{\text{axi}}[w_h] + \mathbf{f}_a^{\text{axi}}[w_h] + \lambda_h \mathbf{G}^{\text{axi}}[w_h] \quad 1 \le a \le n+1, \tag{A.1a}$$

$$\text{where} \quad \mathbf{F}_a^{\text{axi}} = \delta_a \Pi_B^{\text{axi}}[w_h] = \frac{\kappa_b}{2} \int_I \left(2\mathrm{H}_{\text{axi}} \mathrm{J}_{\text{axi}}\, \delta_a \mathrm{H}_{\text{axi}} + \mathrm{H}_{\text{axi}}^2 \delta_a \mathrm{J}_{\text{axi}} \right) dt, \tag{A.1b}$$

$$\mathbf{G}_a^{\text{axi}} = \delta_a \Pi_A^{\text{axi}}[w_h] = \int_I \delta_a \mathrm{J}_{\text{axi}}\, dt, \tag{A.1c}$$

$$\mathbf{f}_a^{\text{axi}} = \delta_w \Pi_F^{\text{axi}}[w_h] = \int_I \left(\delta_a \mu\, \mathrm{J}_{\text{axi}} + \mu\, \delta_a \mathrm{J}_{\text{axi}} \right) dt. \tag{A.1d}$$

The linearizations $\delta_a(\cdot)$ appearing in (A.1) follow from definitions (50) as

$$
\begin{aligned}
\delta_a r &= N_{a,p}\,(\mathbf{n}_0\cdot\mathbf{e}_r)\\
\delta_a r' &= (N'_{a,p}\mathbf{n}_0 + N_{a,p}\mathbf{n}'_0)\cdot\mathbf{e}_r\\
\delta_a r'' &= (N''_{a,p}\mathbf{n}_0 + 2N'_{a,p}\mathbf{n}'_0 + N_{a,p}\mathbf{n}''_0)\cdot\mathbf{e}_r\\
\delta_a z &= N_{a,p}\,(\mathbf{n}_0\cdot\mathbf{e}_z)\\
\delta_a z' &= (N'_{a,p}\mathbf{n}_0 + N_{a,p}\mathbf{n}'_0)\cdot\mathbf{e}_z\\
\delta_a z'' &= (N''_{a,p}\mathbf{n}_0 + 2N'_{a,p}\mathbf{n}'_0 + N_{a,p}\mathbf{n}''_0)\cdot\mathbf{e}_z\\
\delta_a\alpha &= z''\delta_a r' + r'\delta_a z'' - z'\delta_a r'' - r''\delta_a z'\\
\delta_a\beta &= \frac{r'\delta_a r' + z'\delta_a z'}{\beta}\\
\delta_a \mathrm{J}_{\mathrm{axi}} &= 2\pi\,(\beta\delta_a r + r\delta_a\beta)\\
\delta_a \mathrm{H}_{\mathrm{axi}} &= -\frac{\mathrm{H}_{\mathrm{axi}}}{\beta}\delta_a\beta + \frac{1}{\beta^2}\left(\delta_a\alpha - \frac{\alpha}{\beta}\delta_a\beta\right) + \frac{1}{\beta r}\left(\delta_a z' - \frac{z'}{r}\delta_a r\right)\\
\delta_a\mu &= \frac{\partial\mu}{\partial r}\delta_a r + \frac{\partial\mu}{\partial z}\delta_a z.
\end{aligned}
\tag{A.2}
$$

A.2. Evaluation of tangents

The tangent matrix $\mathbf{A}^{\mathrm{axi}}$ is the consistent linearization of the residual $\mathbf{R}^{\mathrm{axi}}$, namely,

$$
\mathbf{A}^{\mathrm{axi}}[w_h,\lambda_h] = \begin{bmatrix} \mathbf{K}^{\mathrm{axi}}[w_h] + \mathbf{L}^{\mathrm{axi}}[w_h] + \lambda_h\mathbf{M}^{\mathrm{axi}}[w_h] & \mathbf{G}^{\mathrm{axi}}[w_h] \\ \mathbf{G}^{\mathrm{axi}}[w_h]^{\mathrm{T}} & 0 \end{bmatrix},
\tag{A.3}
$$

where $\mathbf{K}^{\mathrm{axi}}$, $\mathbf{L}^{\mathrm{axi}}$ and $\mathbf{M}^{\mathrm{axi}}$ are the linearizations of $\mathbf{F}^{\mathrm{axi}}$, $\mathbf{f}^{\mathrm{axi}}$ and $\mathbf{G}^{\mathrm{axi}}$, respectively. Denoting $\delta^2_{ab}(\cdot) := \langle\delta^2(\cdot), N_{a,p}, N_{b,p}\rangle$, their components are derived from (A.1) as

$$
\begin{aligned}
\mathbf{K}^{\mathrm{axi}}_{ab} = \delta^2_{ab}\Pi^{\mathrm{axi}}_B[w_h] = \kappa_b\int_I \Big[&\Big(\delta_b\mathrm{H}_{\mathrm{axi}}\,\delta_a\mathrm{H}_{\mathrm{axi}} + \mathrm{H}_{\mathrm{axi}}\,\delta^2_{ab}\mathrm{H}_{\mathrm{axi}}\Big)\mathrm{J}_{\mathrm{axi}} + \\
&+ (\delta_b\mathrm{J}_{\mathrm{axi}}\,\delta_a\mathrm{H}_{\mathrm{axi}} + \delta_a\mathrm{J}_{\mathrm{axi}}\,\delta_b\mathrm{H}_{\mathrm{axi}})\,\mathrm{H}_{\mathrm{axi}} + \frac{\mathrm{H}^2_{\mathrm{axi}}}{2}\delta^2_{ab}\mathrm{J}_{\mathrm{axi}}\Big]dt,
\end{aligned}
\tag{A.4a}
$$

$$
\mathbf{M}^{\mathrm{axi}}_{ab} = \delta^2_{ab}\Pi^{\mathrm{axi}}_A[w_h] = \int_I \delta^2_{ab}\mathrm{J}_{\mathrm{axi}}\,dt,
\tag{A.4b}
$$

$$
\mathbf{L}^{\mathrm{axi}}_{ab} = \delta^2_{ab}\Pi^{\mathrm{axi}}_F[w_h] = \int_I \Big(\delta^2_{ab}\mu\,\mathrm{J}_{\mathrm{axi}} + \delta_a\mu\,\delta_b\mathrm{J}_{\mathrm{axi}} + \delta_b\mu\,\delta_a\mathrm{J}_{\mathrm{axi}} + \mu\,\delta^2_{ab}\mathrm{J}_{\mathrm{axi}}\Big)\,dt.
\tag{A.4c}
$$

The second variations $\delta^2_{ab}(\cdot)$ appearing in (A.4) are in turn computed using (50) and (A.2) as

$$
\begin{aligned}
\delta^2_{ab} r &= \delta^2_{ab} r' = \delta^2_{ab} r'' = \delta^2_{ab} z = \delta^2_{ab} z' = \delta^2_{ab} z'' = 0\\
\delta^2_{ab}\alpha &= \delta_a r'\delta_b z'' + \delta_a z''\delta_b r' - \delta_a r''\delta_b z' - \delta_a z'\delta_b r''\\
\delta^2_{ab}\beta &= \frac{1}{\beta}\left(\delta_a r'\delta_b r' + \delta_a z'\delta_b z' - \delta_a\beta\delta_b\beta\right)\\
\delta^2_{ab}\mathrm{J}_{\mathrm{axi}} &= 2\pi\left(\delta_a r\delta_b\beta + \delta_a\beta\delta_b r + r\delta^2_{ab}\beta\right)\\
\delta^2_{ab}\mathrm{H}_{\mathrm{axi}} &= -\frac{\delta_a\mathrm{H}_{\mathrm{axi}}\delta_b\beta}{\beta} - \frac{1}{\beta^2}\left(\delta_a\beta\delta_b\mathrm{H}_{\mathrm{axi}} + \mathrm{H}_{\mathrm{axi}}\delta^2_{ab}\beta\right)\\
&\quad + \frac{1}{\beta^2}\left(\delta^2_{ab}\alpha - \frac{\delta_a\beta\delta_b\alpha + \alpha\delta^2_{ab}\beta}{\beta} + \frac{\alpha\delta_a\beta\delta_b\beta}{\beta^2}\right) - \frac{\delta_b\beta}{\beta^3}\left(\delta_a\alpha - \frac{\alpha}{\beta}\delta_a\beta\right)\\
&\quad + \frac{2z'}{\beta r^3}\delta_a r\delta_b r - \frac{1}{\beta r^2}\left(\delta_a r\delta_b z' + \delta_a z'\delta_b r\right)\\
\delta^2_{ab}\mu &= \frac{\partial^2\mu}{\partial^2 r}\delta_a r\delta_b r + \frac{\partial^2\mu}{\partial^2 z}\delta_a z\delta_b z + \frac{\partial^2\mu}{\partial r\partial z}\left(\delta_a r\delta_b z + \delta_a z\delta_b r\right).
\end{aligned}
$$

References

[1] W. Helfrich, Elastic properties of lipid bilayers: theory and possible experiments, Z. Naturforsch. Teil C, Biochem. Biophys. Biol. Virol. 28 (11) (1973) 693.
[2] J. Jenkins, The equations of mechanical equilibrium of a model membrane, SIAM J. Appl. Math. 32 (4) (1977) 755–764.
[3] D. Steigmann, Fluid films with curvature elasticity, Arch. Ration. Mech. Anal. 150 (2) (1999) 127–152.
[4] J. Nitsche, Boundary value problems for variational integrals involving surface curvatures, Quart. Appl. Math. 51 (1993) 363–387.
[5] P. Canham, The minimum energy of bending as a possible explanation of the biconcave shape of the human red blood cell, J. Theor. Biol. 26 (1) (1970) 61–81.
[6] U. Seifert, Configurations of fluid membranes and vesicles, Adv. Phys. 46 (1) (1997) 13–137.
[7] P. Bassereau, B. Sorre, A. Lévy, Bending lipid membranes: experiments after W. Helfrich's model, Adv. Colloid Interface Sci. 208 (2014) 47–57.
[8] J. Jenkins, Static equilibrium configurations of a model red blood cell, J. Math. Biol. 4 (2) (1977) 149–169.
[9] A. Agrawal, D.J. Steigmann, Boundary-value problems in the theory of lipid membranes, Contin. Mech. Thermodyn. 21 (1) (2009) 57–82.
[10] J. Luke, A method for the calculation of vesicle shapes, SIAM J. Appl. Math. 42 (2) (1982) 333–345.
[11] L. Shampine, J. Kierzenka, M. Reichelt, Solving boundary value problems for ordinary differential equations in Matlab with BVP4C, in: Tutorial Notes, 2000, pp. 437–448.
[12] Q. Du, C. Liu, X. Wang, A phase field approach in the numerical study of the elastic bending energy for vesicle membranes, J. Comput. Phys. 198 (2) (2004) 450–468.
[13] T. Biben, K. Kassner, C. Misbah, Phase-field approach to three-dimensional vesicle dynamics, Phys. Rev. E 72 (4) (2005) 041921.
[14] A. Rosolen, C. Peco, M. Arroyo, An adaptive meshfree method for phase-field models of biomembranes. Part I: approximation with maximum-entropy basis functions, J. Comput. Phys. 249 (2013) 303–319.
[15] Q. Du, C. Liu, X. Wang, Simulating the deformation of vesicle membranes under elastic bending energy in three dimensions, J. Comput. Phys. 212 (2) (2006) 757–777.
[16] Q. Du, J. Zhang, Adaptive finite element method for a phase field bending elasticity model of vesicle membrane deformations, SIAM J. Sci. Comput. 30 (3) (2008) 1634–1657.
[17] K. Deckelnick, G. Dziuk, C. Elliott, Computation of geometric partial differential equations and mean curvature flow, Acta Numer. 14 (2005) 139–232.
[18] F. Feng, W. Klug, Finite element modeling of lipid bilayer membranes, J. Comput. Phys. 220 (1) (2006) 394–408.
[19] L. Ma, W. Klug, Viscous regularization and r-adaptive remeshing for finite element analysis of lipid membrane mechanics, J. Comput. Phys. 227 (11) (2008) 5816–5835.
[20] E. Bänsch, P. Morin, R. Nochetto, A finite element method for surface diffusion: the parametric case, J. Comput. Phys. 203 (1) (2005) 321–343.
[21] J. Barrett, H. Garcke, R. Nürnberg, Parametric approximation of Willmore flow and related geometric evolution equations, SIAM J. Sci. Comput. 31 (1) (2008) 225–253.
[22] M. Arroyo, A. DeSimone, Relaxation dynamics of fluid membranes, Phys. Rev. E 79 (3) (2009) 031915.
[23] M. Rahimi, M. Arroyo, Shape dynamics, lipid hydrodynamics, and the complex viscoelasticity of bilayer membranes, Phys. Rev. E 86 (1) (2012) 011932.
[24] I. Tasso, G. Buscaglia, A finite element method for viscous membranes, Comput. Methods Appl. Mech. Eng. 255 (2013) 226–237.
[25] A. Bonito, R. Nochetto, P. Sebastian, Parametric FEM for geometric biomembranes, J. Comput. Phys. 229 (9) (2010) 3171–3188.
[26] G. Dziuk, Computational parametric Willmore flow, Numer. Math. 111 (1) (2008) 55–80.
[27] R.E. Rusu, An algorithm for the elastic flow of surfaces, Interfaces Free Bound. 7 (3) (2005) 229–239.
[28] T. Hughes, J.A. Cottrell, Y. Bazilevs, Isogeometric analysis: CAD, finite elements, NURBS, exact geometry and mesh refinement, Comput. Methods Appl. Mech. Eng. 194 (39) (2005) 4135–4195.
[29] H. Gómez, V. Calo, Y. Bazilevs, T. Hughes, Isogeometric analysis of the Cahn–Hilliard phase-field model, Comput. Methods Appl. Mech. Eng. 197 (49) (2008) 4333–4352.
[30] M. Bloor, M. Wilson, Method for efficient shape parametrization of fluid membranes and vesicles, Phys. Rev. E 61 (4) (2000) 4218.
[31] D. Steigmann, E. Baesu, R. Rudd, J. Belak, M. McElfresh, On the variational theory of cell-membrane equilibria, Interfaces Free Bound. 5 (2003) 357–366.
[32] R. Capovilla, J. Guven, E. Rojas, Hamilton's equations for a fluid membrane, J. Phys. A 38 (2005) 8841.
[33] T.J. Healey, S. Dharmavaram, Existence of global symmetry-breaking solutions in an elastic phase-field model for lipid bilayer vesicles, arXiv preprint, arXiv:1402.2314.
[34] H. Gao, W. Shi, L. Freund, Mechanics of receptor-mediated endocytosis, Proc. Natl. Acad. Sci. USA 102 (27) (2005) 9469–9474.
[35] S. Zhang, J. Li, G. Lykotrafitis, G. Bao, S. Suresh, Size-dependent endocytosis of nanoparticles, Adv. Mater. 21 (4) (2009) 419–424.
[36] L. Chou, K. Ming, W. Chan, Strategies for the intracellular delivery of nanoparticles, Chem. Soc. Rev. 40 (1) (2011) 233–245.
[37] A. Albanese, P. Tang, W. Chan, The effect of nanoparticle size, shape, and surface chemistry on biological systems, Annu. Rev. Biomed. Eng. 14 (2012) 1–16.
[38] X. Shi, A. von dem Bussche, R. Hurt, A. Kane, H. Gao, Cell entry of one-dimensional nanomaterials occurs by tip recognition and rotation, Nat. Nanotechnol. 6 (11) (2011) 714–719.
[39] Y. Li, H. Yuan, A. von dem Bussche, M. Creighton, R. Hurt, A. Kane, H. Gao, Graphene microsheets enter cells through spontaneous membrane penetration at edge asperities and corner sites, Proc. Natl. Acad. Sci. USA 110 (30) (2013) 12295–12300.
[40] H. Gao, Probing mechanical principles of cell–nanomaterial interactions, J. Mech. Phys. Solids 62 (2014) 312–339.
[41] L. Wilson, P. Matsudaira, M. Sheetz, Laser Tweezers in Cell Biology, Methods Cell Biol., vol. 55, Academic Press, 1997.
[42] M. Do Carmo, Differential Geometry of Curves and Surfaces, vol. 2, Prentice Hall, Englewood Cliffs, 1976.
[43] U. Seifert, R. Lipowsky, Morphology of vesicles, in: Handbook of Biological Physics, vol. 1, 1995, pp. 403–464.
[44] S. Balay, S. Abhyankar, M. Adams, J. Brown, P. Brune, K. Buschelman, V. Eijkhout, W. Gropp, D. Kaushik, M. Knepley, L. McInnes, K. Rupp, B. Smith, H. Zhang, PETSc users manual, Tech. Rep. ANL-95/11 – Revision 3.4, Argonne National Laboratory, 2013, http://www.mcs.anl.gov/petsc.
[45] M. Galassi, J. Davies, J. Theiler, B. Gough, G. Jungman, M. Booth, F. Rossi, GNU scientific library reference manual, ISBN 0954161734, http://www.gnu.org/software/gsl.
[46] C. de Boor, A Practical Guide to Splines, Appl. Math. Sci., Springer, New York, 1978.
[47] S. Brenner, R. Scott, The Mathematical Theory of Finite Element Methods, Texts Appl. Math., vol. 15, Springer, 2008.
[48] U. Seifert, Adhesion of vesicles in two dimensions, Phys. Rev. A 43 (12) (1991) 6803.
[49] W. Shi, X.Q. Feng, H. Gao, Two-dimensional model of vesicle adhesion on curved substrates, Acta Mech. Sin. 22 (6) (2006) 529–535.
[50] X. Xu, A. Needleman, Numerical simulations of fast crack growth in brittle solids, J. Mech. Phys. Solids 42 (9) (1994) 1397–1434.
[51] J.N. Israelachvili, Intermolecular and Surface Forces, revised third edition, Academic Press, 2011.
[52] M. Deserno, Elastic deformation of a fluid membrane upon colloid binding, Phys. Rev. E 69 (3) (2004) 031903.
[53] M. Deserno, T. Bickel, Wrapping of a spherical colloid by a fluid membrane, Europhys. Lett. 62 (5) (2003) 767.
[54] W. Gózdz, Deformations of lipid vesicles induced by attached spherical particles, Langmuir 23 (10) (2007) 5665–5669.
[55] L. Freund, Y. Lin, The role of binder mobility in spontaneous adhesive contact and implications for cell adhesion, J. Mech. Phys. Solids 52 (11) (2004) 2455–2472.

[56] L. Freund, The stiffness of a biomembrane force probe vesicle, Math. Mech. Solids 14 (1–2) (2009) 148–160.
[57] I. Derényi, F. Jülicher, J. Prost, Formation and interaction of membrane tubes, Phys. Rev. Lett. 88 (23) (2002) 238101.
[58] T. Powers, G. Huber, R. Goldstein, Fluid-membrane tethers: minimal surfaces and elastic boundary layers, Phys. Rev. E 65 (4) (2002) 041901.
[59] P. Mattila, P. Lappalainen, Filopodia: molecular architecture and cellular functions, Nat. Rev. Mol. Cell Biol. 9 (6) (2008) 446–454.
[60] M. Elbaum, D. Fygenson, A. Libchaber, Buckling microtubules in vesicles, Phys. Rev. Lett. 76 (21) (1996) 4078.
[61] A. Shibuya, Y. Saito, H. Hyuga, Morphology of axisymmetric vesicles with encapsulated filaments and impurities, J. Phys. Soc. Jpn. 71 (7) (2002) 1780–1788.
[62] C. Huang, Y. Zhang, H. Yuan, H. Gao, S. Zhang, Role of nanoparticle geometry in endocytosis: laying down to stand up, Nano Lett. 13 (9) (2013) 4546–4550.
[63] X. Yi, H. Gao, Phase diagrams and morphological evolution in wrapping of rod-shaped elastic nanoparticles by cell membrane: a two-dimensional study, Phys. Rev. E 89 (6) (2014) 062712.
[64] P. Decuzzi, M. Ferrari, The receptor-mediated endocytosis of nonspherical particles, Biophys. J. 94 (10) (2008) 3790–3797.
[65] P. Decuzzi, R. Pasqualini, W. Arap, M. Ferrari, Intravascular delivery of particulate systems: does geometry really matter?, Pharm. Res. 26 (1) (2009) 235–243.
[66] M. Herant, V. Heinrich, M. Dembo, Mechanics of neutrophil phagocytosis: experiments and quantitative models, J. Cell Sci. 119 (9) (2006) 1903–1913.